UNIVERSITY OF OTTAWA

DOCTORAL THESIS

Interferometric methods for seismic monitoring in industrial environments

Author:

Philippe DALES

Supervisor:

Dr. Pascal AUDET

A thesis submitted in fulfillment of the requirements

for the degree of Doctor of Philosophy in the

Faculty of Science

Department of Earth and Environmental Sciences

October 19, 2018

UNIVERSITY OF OTTAWA

Abstract

Faculty of Science

Department of Earth and Environmental Sciences

Doctor of Philosophy

Interferometric methods for seismic monitoring in industrial environments

by Philippe DALES

As the global demand for energy and natural resources continues to increase so does our interaction with Earth's near surface through resource extraction and waste injection. In monitoring these interaction, seismology plays a central role. The focus of this work is on improving the detection and localization of seismic sources, a fundamental problem in seismology.

After discussing the strengths and limitations of existing methods for source detection and localization, I develop a solution based on a beamforming approach that uses cross-correlation functions in a maximum likelihood search for sources of seismic energy. I call this method InterLoc, short for 'interferometric locator', and apply it to data recorded at two active underground mines to demonstrate its effectiveness in monitoring both impulsive sources and persistent sources. Next, I demonstrate how persistent seismic sources, typically seen as contaminants, can be used directly to measure small changes in the medium

between a source and either source-station pairs. This method relies on the ability to locate and monitor source activity and then use this information to identify and select cross-correlation functions to isolate each source of interest. From the resulting cross-correlations, it is possible to measure small temporal changes in the waveforms. To demonstrate this method, I show how ore-crushers can be used to track the growth of a block cave by measuring changes in traveltimes due to ray paths having to circumvent the growing cave.

In the final chapter I focus on the development of a processing framework for the detection and location of microseismic events recorded on dense (or large-N) surface arrays. The proposed framework involves: (1) data reduction; (2) dividing the array into smaller sub-arrays; (3) waveform processing within fixed time windows; (4) stacking of time windows selected based on each potential origin time and source location; and (6) combining the output from all sub-arrays to infer detections and locations of sources. This methodology is validated with synthetic data built to emulate a real dataset from a 10,050 node survey to evaluate the suitability of land for carbon sequestration. Based on the presence of very strong coherent contaminating sources and low rock quality, I am only able to detect sources with moment magnitude greater than -0.5. In the five hours of data processed there is no positive detections suggesting this could be a good site for carbon storage. More work is needed to improve the detection threshold and quantify risk based on event location and magnitude.

In summary, my work demonstrates how the interference (via cross-correlation) and stacking of seismic waveforms can be combined in different ways to create effective solutions for problems faced by today's industries.

Acknowledgements

I would like to express my sincere gratitude to my advisor Prof. Pascal Audet for his support, advice and patience. I have never met someone so busy yet so generous with their time, I truly could not have asked for a better advisor and mentor for my Ph.D study.

My sincere thanks also goes to Dr. Gerrit Olivier who went far out of his way to collaborate with nothing guaranteed in return. It's difficult to imagine what my project would be like without your involvement and I look forward to working on future projects together.

I am also grateful to Dr. Jean-Philippe Mercier for the introduction to mine seismology and collaboration during the early stages of my project.

Finally, I would like to thank my wonderful parents Johanne and Bob for the endless support and encouragement.

Contents

List of Figures

Chapter 1

Introduction

1.1 Societal context

Population growth and modern societal constructs (e.g. 'new consumers' [1]) continue to increase the global demand for energy and natural resources. Even with the advent of electric vehicles and green energies, aggregate forecasts predict the demand for petroleum will peak somewhere between 2030 and 2040 [2]. On the other hand, the demand for mineral resources, which serve as essential inputs for economic and technological progress, is not expected to slow [3, 4]. In addition, the ongoing extraction of these natural resources has depleted the largest and most easily accessible reserves, making future ventures riskier and less profitable. However, these future supply issues have largely been masked by the current oversupply of raw materials in global markets [3].

Keeping pace has and will require continued innovation in both exploration and extraction of natural resources. Examples of this can be found in the petroleum industry with offshore exploration and shale-gas extraction, and in the mining industry with deeper ore extraction (Mponeng, a gold mine in South Africa extends 4 km below the surface), mass mining methods (e.g. block caving [5]) and

more remote exploration. Private industry has even begun looking to off-world resources in the form of asteroid mining [6, 7].

The by-product of our increased consumption is waste and new methods for its disposal will be required if we wish to continue growing sustainably. Fortunately, the last few decades have seen steady progress in environmental awareness and capital investment into 'green' technologies [8, 9]. While many solid materials can be recycled, it is much more difficult to deal with emissions produced by the combustion of fossil fuels, the primary cause of anthropogenic climate change [8, 9]. One potential solution to curb emissions is carbon capture and sequestration (or storage), abbreviated CCS [10, 11, 12], which involves capturing CO_2 from large emitters (e.g. coal power plants) and injecting it deep underground (typically 1-3 km). Therefore, in addition to being a source of raw materials, Earth's near surface can also be used as a repository for our waste.

Sustainable growth is arguably society's central goal and to achieve it we need improved methods for finding resources, extracting resources and disposing of waste. Improvement in this context means increasing the productivity of these ventures and lowering their overall risk, be it financial, environmental, individual or other.

1.2 Relation to seismology

As society continues to develop, so will our interaction with the first several kilometers of Earth's surface. This interaction requires knowledge of the medium's existing state (exploration) and how it will respond to human activity (monitoring). Measurements of this state can be made either directly through sampling or indirectly through geophysical methods.

Exploration combines direct and indirect measurements to build a static image of the medium's existing state. This process typically involves reducing an initial search area through the following steps: (1) airborne potential field methods; (2) active seismic; and (3) drilling of potential targets for ground-truthing. Potential field methods (e.g. magnetic, gravity) involve detecting anomalies associated with certain ore bodies and hydrocarbon reserves [13]. These methods allow the surveying of large areas at low cost, but their physical nature limits them in terms of depth sensitivity and resolution.

Once a potential target is identified, active seismic is often used to build a high resolution image of the subsurface. In hydrocarbon exploration, the most widely used method is active seismic reflection [14] which involves mapping subsurface reflectors through two-way travel-time measurements of seismic waves generated by active sources (e.g. large vibrating trucks or explosive shots). This technique has also seen some use in mineral exploration in cases where the ore body is much denser than the host rock [15, 16] as the portion of reflected energy depends on the impedance (related to density) contrast at material boundaries. The primary limitation of this method is that the active sources are expensive and difficult to operate in remote or environmentally sensitive areas. Drilling is usually reserved for the final steps in the exploration process due to its high cost and ability to only give point measurements.

Once a viable target of interest has been identified, the extraction (or injection) process begins, during which properties of the rockmass are being actively modified. These different processes upset the static equilibrium (stress, porepressure etc) and in general increase the frequency/severity of seismic activity. One noteable example is the state of Oklahoma in the United States, where

wastewater injection has greatly increased seismicity, even surpassing the state of California [17]. This 'induced' seismicity has led to seismic methods being the standard tool for monitoring processes such as mining [18, 19, 20], hydraulic fracturing [21], geothermal [22, 23] and CO_2 injection [24, 25, 26] through the coupled process of determining the nature (location, rate, energy release) of seismic sources and using this information to infer properties of the rockmass (velocities, stress, fractures, geology).

1.3 Recent developments in seismology

Cheaper electronics, faster computers and wireless technology have led to a world filled with sensors and seismology is no exception, with increasingly dense seismic networks and arrays [see 27, 28, 29, 30, 31, 32] generating overwhelming amounts of data [33]. While the performance and availability of computers is currently able to scale with increasing data volumes, human-hours have not. This has led to a redistribution of these limited hours from the more basic and repetitive tasks (e.g. manual seismic phase picking) to the development of automated processing methods and the interpretation of their output. Unfortunately, the majority of methods are developed to process only a tiny fraction of all recorded data, such as visible earthquake arrival waveforms (i.e. signal-to-noise ratio SNR greater than one). With power law distributions describing the size and frequency of earthquake aftershocks [34], it is likely that for each of these clearly detectable earthquakes, many events of smaller magnitude are also occurring. Detection and location of these weaker events requires processing methods that exploit the coherency of their arrival waveforms recorded

at many independent stations. In this regard, effective processing techniques appear to be lacking with respect to available instrumentation.

Even in the complete absence of sources, the background seismic noise itself can be processed to effectively simulate a source at each station, a technique called ambient noise interferometry [35]. This method involves the cross-correlation of noise recordings between a pair of sensors, where the resulting signal represents the approximate Green's function (i.e. Earth impulse response) of the intervening medium. Due to the almost endless availability of noise recordings obtained from passive and continuously operating seismic stations, this approach has become a standard tool in seismology and has been successfully used to perform surface wave tomography [36, 37, 38, 39], body wave tomography [40] and temporal monitoring of seismic wave velocity changes [41, 42, 19]. The primary limitation of this method is the reliance on a diffuse seismic wavefield (i.e., equipartition of modes) [43, 44, 45], which is typically violated in industrial environments where few strong sources of ground motion produce anisotropic and directional seismic wavefields. Therefore, successful application of this technique relies on being able to evaluate the seismic wavefield in space and time, for which the detection and location of seismic sources is critical.

1.4 Summary of our contribution

The focus of this work is on improving the detection and localization of seismic sources and how these sources can be used to infer properties of the medium. We are especially interested in the application of these methods in industrial environments to guide and improve operations.

1.4.1 Chapter 2

Our first paper, published in Geophysical Journal International in 2017 [20], begins by discussing the strengths and limitations of existing source detection and localization methods. Based on these findings and the recent developments in seismology, the goal was to implement a method that met the following criteria:

1. Automated processing, robust at any time and spatial scale. Time scale referring to determining which sources dominate at short (e.g. microseismic events) and long time scales (e.g. directionality of background wavefield).

2. Able to locate impulsive and persistent sources. This is especially important in industrial environments where contaminating sources (pumps, fans, road traffic) exist.

3. Able to locate simultaneously occurring sources.

4. Implementation that runs on today's computer hardware (i.e. single desktops).

Our solution is based on a popular beamforming-like approach that uses cross-correlation functions in a maximum likelihood search to detect and locate sources of seismic energy. We term this method InterLoc, short for 'interferometric locator'. To illustrate the technique we use a synthetic example in which two simultaneous sources are located, were we briefly discuss the effects of different processing parameters. Next we apply the method to real data recorded at two active underground mines to demonstrate the effectiveness of this technique in monitoring both impulsive sources (micro-earthquakes) and other persistent sources (drilling and ore crushers). We then propose how this information can

be used in conjunction with ambient seismic noise interferometry by identifying and selectively stacking only time periods where wavefield conditions are suitable. Finally, we demonstrate the potential for using stable persistent sources to monitor changing rockmass conditions and guide mining operations.

1.4.2 Chapter 3

Our second paper, published in Geophysical Research Letters in 2017 [46], follows up on the use of persistent sources to perform sensitive temporal monitoring of the rockmass at a block caving mine. The initial goal was to use ambient noise interferometry to turn each station into a virtual source; however, with three nearly continuously operating ore-crushers, the resulting wavefield was very unsuited for this technique. This problem is frequently encountered in applications of ambient noise interferometry where few persistent sources dominate the cross-correlations, resulting in arrivals at non-physical lag times (with respect to inter-station propagating seismic waves).

Instead, we show that these typically contaminating sources can be used directly to measure small changes in the medium between a source and either (or both) source-station pairs. This method relies on the ability to locate and monitor source activity and then use this information to identify and select cross-correlation functions to isolate each source of interest. From the resulting cross-correlations, a simple marching method was used to measure travel-time changes in these waveforms over the 40-day period. We attribute these travel-time changes to the additional path length incurred by the crusher-station ray paths having to circumvent the growing cave.

Although the use of active sources to perform temporal monitoring is not a novel technique, here we are dealing with multiple uncontrolled sources (i.e. sources for which we cannot control the location and/or source-time function). We illustrate this technique by using three nearly continuously operating ore-crushers to track the growth of a block cave at an underground mine. This technique should work equally well in natural environments using sources such as volcanic tremor, hydrothermal bubble cavitation and microseisms.

1.4.3 Chapter 4

In the final chapter (paper to be submitted), we develop a processing framework for the detection and location of microseismic events recorded on dense surface arrays. These types of single-component temporary nodal array deployments are becoming increasingly popular due to their low cost.

We begin by reviewing existing work in this domain, highlighting the strengths and limitations of different approaches. Based on this information, we propose our own framework, which involves: (1) decimating and stacking waveforms at adjacent stations to reduce data volume; (2) dividing the array into smaller sub-arrays (patches) to exploit local waveform similarity; (3) dividing and processing the waveforms within fixed time windows; (4) selecting the appropriate time windows based on each potential origin time and source location; (5) stacking the selected waveforms; and (6) combining the output from all patches to infer detections and locations of sources. This processing framework is illustrated using a synthetic example and is shown to be robust even in the case where the signal-to-noise ratio on single waveforms is well below one.

Next we apply this processing to a real dataset resulting from a 10,050 node survey that was deployed to evaluate the suitability of a 3×3 km^2 piece of land for carbon sequestration. Using these data, we identify contaminant sources that dominate the waveforms, such as vehicles traveling along highways surrounding the array and acoustic waves produced by nearby pumping stations. The coherent signals created by these sources can potentially bias the recovery of true microseismic events, and we propose a method to minimize these artifacts. Based on the presence of these contaminating sources and low rock quality, we are only able to detect sources with moment magnitude greater than -0.5. In the five hours of data processed there is no positive detections suggesting this could be a good site for carbon storage however we can not rule out the possibility of weaker events which could still pose a leakage risk.

Although we have summarized our findings so far, this research is still in progress. Apart from processing the remaining portions of the dataset, more work is needed to improve the removal of coherent contaminating sources that severely limit the detection threshold of microseismic events. Possible solutions include burying the sensors to reduce contamination by acoustic waves propagating in the air, or placing microphones at each pumping station to record and deconvolve the associated source-time functions.

Chapter 2

Interferometric methods for spatio-temporal seismic monitoring in underground mines

Philippe Dales[1], Pascal Audet[1], Gerrit Olivier[2], Jean-Philippe Mercier[3],

[1]Department of Earth and Environmental Sciences, University of Ottawa

[2]Institute of Mine Seismology, Hobart, Tasmania

[3]Oyu Tolgoi Mine, Khanbogd, Mongolia

A version of this chapter has been published. P. Dales, P. Audet, G. Olivier, and J.-P. Mercier. Interferometric methods for spatio-temporal monitoring in underground mines. *Geophysical Journal International*, 210, 731-742, 2017.

2.1 Summary

In active underground mining environments, monitoring of the rockmass has important implications for both safety and productivity. Monitoring can be accomplished by exploiting the many passive seismic sources (microearthquakes, drilling, ore-crushers etc.) around the mine on the condition they can be accurately detected and located. We implement a popular beamforming-like approach that uses cross-correlation functions in a maximum likelihood search to locate sources of seismic energy. We illustrate the technique with a synthetic example in which two simultaneous sources are located and discuss briefly the effects of different processing parameters. We demonstrate the effectiveness of this technique by monitoring both impulsive sources (microearthquakes) and other persistent sources (drilling and ore-crushers) in two active underground mines. We then propose how this information can be used in conjunction with ambient seismic noise interferometry to estimate seismic Green's functions under temporally variable and anisotropic wavefield conditions. Alternatively, we demonstrate how stable persistent sources, typically seen as contaminants in ambient noise applications, can be used to monitor changing rockmass conditions and potentially guide mining operations.

2.2 Introduction

Automated detection and location of seismic sources is a fundamental problem in seismology, with practical applications for monitoring and earthquake early warning [e.g., 47]. Traditionally, due to the impulsive nature of earthquake rupture, detection has been accomplished using some type of triggering scheme [e.g., 48] while location has involved inverting P- and S-phase arrival times picked at multiple sensors [49]. Although effective at detecting single impulsive sources, phase-picking methods perform poorly when sources are weak relative to background noise, or during periods containing multiple sources, and fail completely in detecting and locating persistent sources where onset times cannot be identified.

In the case of weak or persistent sources, cross-correlation techniques allow for the measurement of time difference of arrivals (or time delays) between pairs of stations. The time delays are estimated by picking the lag time of the maximum peak in the cross-correlated waveforms [50]. The delay time for each station pair corresponds to a hyperbolic curve in 2D (or a paraboloid in 3D) along which the source is likely to lie. These curves are then computed for multiple station pairs with their optimal intersection point giving the best estimate of source location [51]. In seismology, this method has been used for example to locate both non-volcanic tremor within slow earthquakes [52] and the primary origin of the 26-s microseism from ambient noise correlations [53]. The primary drawback to this method is that using only a single peak value in the cross-correlation function leads to failure under strongly scattering conditions or time periods when multiple sources are active. One method found to increase the robustness of the time-delay locator under noisy and reverberant conditions is

by equally weighting all frequencies of the cross-correlation functions [50].

Under conditions where it is difficult (or incorrect in the multi-source case) to pick single arrival times from the original waveforms, or single time delays from the cross-correlated waveforms, beamforming techniques offer a robust solution. Instead of inverting for specific arrival times, beamforming involves phase-delaying and stacking waveforms for each possible source location based on travel times calculated from that location to each station. This is effectively a grid search where the point with the highest stacked amplitude represents the most probable source location. Optimality and variations of this procedure were originally proposed by Hahn and Tretter [54] and then extended to the multiple source case by Wax and Kailath [55].

It should be noted that beamforming techniques can also be thought of as part of a more general framework called matched-field processing (MFP), originally introduced by Bucker [56] for passive target localization (e.g., submarines) in underwater acoustics. MFP involves the systematic comparison of data recorded on a sensor array with synthetic data generated by a wave propagation model. At each potential location, the forward model is compared to the real data, resulting in a probability map of potential source locations. This comparison is most commonly done using the Bartlett processor which correlates the real and synthetic data [57]. In this framework, beamforming can be thought of as the special case where the synthetic signals are appropriately shifted delta functions. Some examples of direct applications of MFP in seismology include locating bubble collapse events to map hydrothermal systems [e.g., 58] and locating microearthquakes buried in anthropogenic noise associated with hydrocarbon extraction [e.g., 59].

Beamforming can be accomplished either using the original or cross-correlated waveforms by simply changing how the delay times (required for signal shifting) are calculated. Using the original waveforms, the appropriate delay times are the direct travel times between each station and the potential source location (see for example the source scanning algorithm by Kao and Shan [60] to locate non-volcanic tremor events in Northern Cascadia). When beamforming using cross-correlated waveforms, the delay times are instead calculated as the difference in travel times from the source location to each station in the pair. This method of time-delay beamforming appears to have been discovered independently many times and is also referred to as beamforming along diffraction hyperbolas [61], steered response power with phase transform (SRP-PHAT) [62, 63], the source scanning algorithm [64, 65] (same name but different method than Kao and Shan [60]) and cross-correlation beamforming [66]. As with the time-delay locator, the cross-correlations are often spectrally whitened prior to localization to decrease the sensitivity of the method to environmental conditions [63]. This method of beamforming using spectrally whitened cross-correlations is robust, intuitive and easy to implement. To simplify the terminology (and hopefully appeal to the ambient noise community) we refer to this technique as an interferometric locator or InterLoc for short.

While we refer to interferometric methods as techniques involving the interference of waveforms through cross-correlation, the term 'seismic interferometry' typically refers to the cross-correlation and summation of seismograms to create virtual events, a technique pioneered by Claerbout [35]. It has since been demonstrated that cross-correlations of ambient seismic noise can be used to construct estimates of the Green's function between sensor pairs, effectively

turning each sensor into a virtual source [36, 37, 38, 39]. Since sensor positions are generally fixed, ambient noise interferometry allows for very sensitive monitoring of temporal velocity changes in the medium between the sensor pair [41, 42]. One of the primary limitations of this method is the reliance on either a fully diffuse wavefield (i.e., equipartition of modes) or a homogeneous distribution of spectrally white noise sources [43, 44], although these conditions can be relaxed slightly in the presence of scatterers, which act as secondary sources [45]. In active underground mines, where few strong sources produce anisotropic and directional wavefields, conditions are generally not suitable to estimate seismic Green's functions [40]. It is possible, however, to isolate periods where conditions are suitable by exploiting the temporal and spatial variability in the wavefield. In this case, an effective technique to monitor the seismic wavefield becomes essential.

In this paper we describe the interferometric locator and show its potential for spatio-temporal monitoring in underground mines. To illustrate the technique we use a synthetic example in which two sources are generated simultaneously. Next, we present the challenges and propose solutions to effectively detect and locate different types of seismic sources. Following from this, we use data recorded at two active underground mines to demonstrate the robustness of this technique by monitoring both impulsive (microearthquakes) and persistent sources (drilling and ore crushers). We then propose integrating seismic monitoring with ambient noise interferometry to improve estimates of seismic Green's functions under temporally variable and anisotropic wavefield conditions. Lastly, we demonstrate the potential of using stable persistent sources to monitor changing rockmass conditions and guide mining operations.

2.3 The interferometric locator

Mathematical expression of the InterLoc method begins with the cross-correlation $C_{12}(t)$ of two signals, $u_1(t)$ and $u_2(t)$, recorded at separate sensors and expressed in the frequency domain as

$$C_{12}(t) = \mathcal{F}^{-1}[\Psi_{12}(\omega)U_1(\omega)U_2^*(\omega)], \tag{2.1}$$

where $\mathcal{F}^{-1}$ is the inverse Fourier transform, $U_1(\omega)$ and $U_2(\omega)$ are the Fourier transforms of $u_1(t)$ and $u_2(t)$, ω is angular frequency, and $\Psi(\omega)$ is the spectral weighting (whitening) coefficient,

$$\Psi_{12}(\omega) = \frac{1}{|U_1(\omega)U_2^*(\omega)|}. \tag{2.2}$$

Then to evaluate the likelihood P of a seismic source being located at point $\vec{q} = (x, y, z)$ we compute all cross-correlations for N sensor pairs, delay them with respect to $\vec{q}$ and sum the zero lag samples according to

$$P(\vec{q}) = \sum_{i=1}^{N} \sum_{j=i+1}^{N} C_{ij}(\tau_i - \tau_j), \tag{2.3}$$

where N is number of sensors and τ_n is the travel time from location $\vec{q}$ to sensor n. We refer to the function P normalized by total number cross-correlations (N choose 2 for unique sensor pair combinations) as the output power, while P evaluated at some point $\vec{q}$ in space is referred to as a functional evaluation (FE) for that given point. By computing FEs at every point in space, the most likely

source location $\vec{q}_s$ is then given where the output power is maximum

$$\vec{q}_s = argmax[P(\vec{q})]. \tag{2.4}$$

2.4 Synthetic example

To illustrate the location technique, we use synthetic data generated with the Salvus spectral element wave propagation package [67]. The simulation setup (Figure 2.1 left panel) consists of a 100×100 m (0.3 m grid spacing) 2D scalar medium in which displacement is recorded at 16 pseudo-randomly located sensors. This geometry attempts to emulate the non-uniform spatial distribution of sensors typical of seismic systems in underground mines. The two synthetic sources have source-time functions corresponding to a microearthquake and ore crusher respectively (Figure 2.1) and have been normalized to have equal energy. An example of the resulting synthetic recordings (spectrally whitened) at two sensors, as well as their cross-correlation, are shown in the left panel of Figure 2.2. Note how each peak in the cross-correlated waveform corresponds to a unique source. Before computing the output power, the CCFs are smoothed using a sliding window root-mean-square with a window length of 0.2 ms (see Section 2.5.2).

The right panel of Figure 2.2 demonstrates how this single cross-correlation function (CCF) is mapped out into space. With a constant velocity model (i.e., straight propagation paths or rays), each lag time in the cross-correlation maps out to a parabola in 2D space along which the time difference of arrival remains constant. Therefore, a peak in correlation at a given lag time indicates that a source is likely to lie somewhere along the parabola associated with that lag

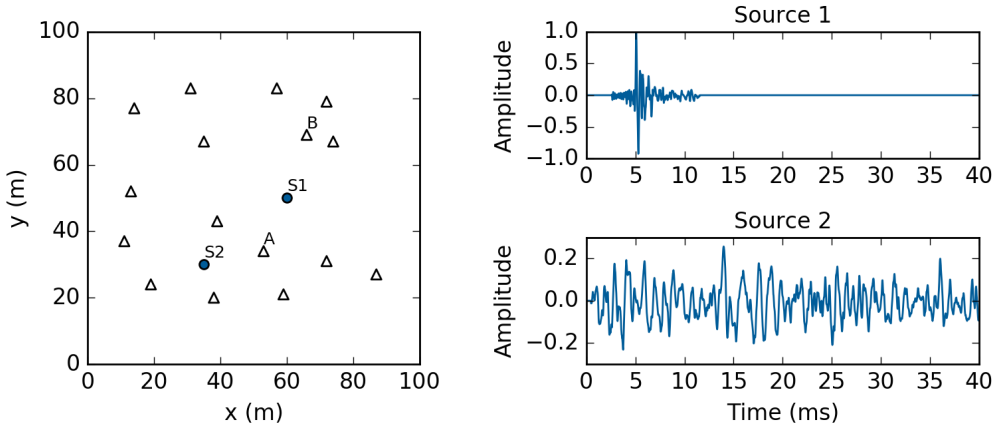

FIGURE 2.1: Left: Geometry of sensors (triangles) and sources (circles) used in the wave propagation simulation. Right: The source-time functions for the two sources which are modeled after a microearthquake (source 1) and an active ore crusher (source 2) respectively.

time. With one pair this provides minimal constraint on location, but after computing and summing the output power for many sensor pairs the true source locations are naturally revealed (Figure 2.3). In the summing process, the non-spurious correlations in each CCF stack constructively, while the spurious correlations, which are not spatially coherent between CCFs, do not.

In this example, the only free parameter is the velocity of the medium, known to be 3000 m/s; however the method remains robust even under poorly estimated velocity models. Estimating and improving the velocity model can be accomplished using the InterLoc method itself as the correct velocity will produce the most focused maximum likelihood volumes. In a constant velocity medium, the optimal value can be obtained by iteratively adjusting the velocity model and recalculating the output power until the global maximum is found, as demonstrated in Figure 2.4.

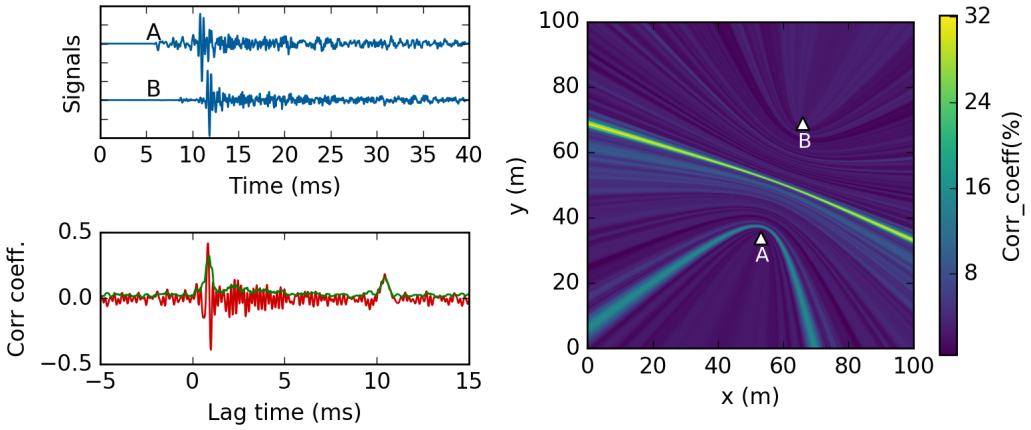

FIGURE 2.2: Left: Example of the synthetic recordings at sensors A and B (top) and the resulting cross-correlation of the two waveforms (bottom). Green solid line in bottom plot is the smoothed signal used in computing the output power. Right: Mapping of the cross-correlation into 2D space assuming a constant velocity model. Each lag time in the CCF corresponds to a parabola in space along which the correlation value is directly mapped. At any point along a parabola the difference in travel time (distance) to each sensor remains constant.

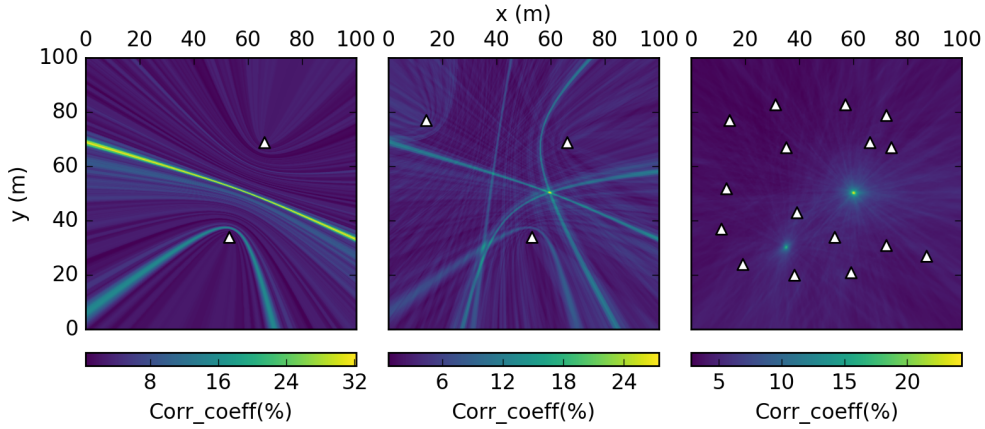

FIGURE 2.3: Effect of mapping out the cross-correlations of the synthetic seismograms in space and summing the resulting output power for 2 (left), 3 (middle) and 16 (right) sensors. Note the peaks in output power at the true source locations.

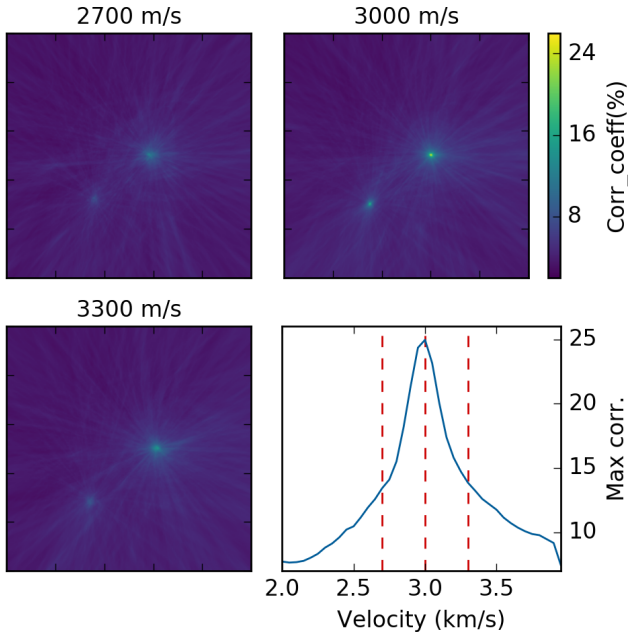

FIGURE 2.4: The effect of the chosen velocity model on the output power for the synthetic dataset. Bottom right panel shows how the maximum correlation value (for the middle source) varies depending on the velocity model used to compute traveltime differences. The peak at 3000 m/s corresponds to the true velocity model used to create the simulation. This behavior can be used to estimate and improve velocity models. Grid dimensions are the same as in Figures 2.2 and 2.3

2.5 Practical implementation and considerations

Similar to ambient noise interferometry, this location method entails computing a set of CCFs semi-continuously in time within finite length windows. Depending on the application, sources can either be located within each time window (e.g., transient impulsive sources) or from the final stacked cross-correlations (e.g., weak and persistent sources). While computing correlations using a long window length is roughly equivalent to stacking several shorter time periods (in the absence of time-domain normalization and spectral whitening), there are many practical advantages to the latter. For each continuous data section the basic processing steps are:

1. Pre-process recordings for each sensor
2. Cross-correlate recordings for all unique sensor pairs
3. Smooth the resulting CCFs
4. Compute functional evaluations

2.5.1 Pre-processing to isolate source contributions

Pre-processing of the data includes splitting data into time-windowed segments, tapering the edges, spectral whitening and bandpass filtering. In cases where multiple sources overlap in time, the resulting output power will be a superposition of probabilities, which leads to ambiguity in the final locations. Effectively isolating a single source type, by maximizing its spatial coherence across the sensor array relative to other sources, can help to reduce this ambiguity. Important parameters to consider when trying to isolate the contribution of the source

of interest to the CCFs are: 1) the window length used to compute the cross-correlations; 2) time-domain normalization; and 3) frequency filtering. Settings for these parameters depend on source characteristics and the purpose of monitoring.

Determining the optimal window length involves achieving a sufficient level of spatial coherence while also limiting temporal and spatial decorrelation. Temporal decorrelation refers to non-stationarity of the source-time function (e.g., feeding of rock to ore crusher stops) and acts to reduce power at the true source location. Spatial decorrelation, on the other hand, refers to the source changing its location (e.g., moving vehicle) within the time window and leads to smearing of the focal volume and reduced output power. Equivalently, a rapidly changing medium could also be responsible for both types of decorrelation.

For the straightforward case of isolating a single impulsive source, coherence is maximized by choosing a window length equal to the duration of the source of interest plus an additional travel time allowance (determined by maximum source-sensor spacing) to ensure the arrival waveform is not clipped at the furthest sensors. This effect can be seen in the middle panel of Figure 2.5 where using a narrower time window (15 ms) centered on the microearthquake significantly increases its relative output power. When trying to isolate a persistent source on the other hand, the window length needs to be long enough to achieve a sufficient level of coherence compared to the other sources present. This effect can be seen in the greater relative contribution from the persistent source (compared to the microearthquake) using the original window length (Figure 2.5 left panel). As long as the persistent source remains in the same location (hence no spatial decorrelation) the upper limit on the window length will be determined

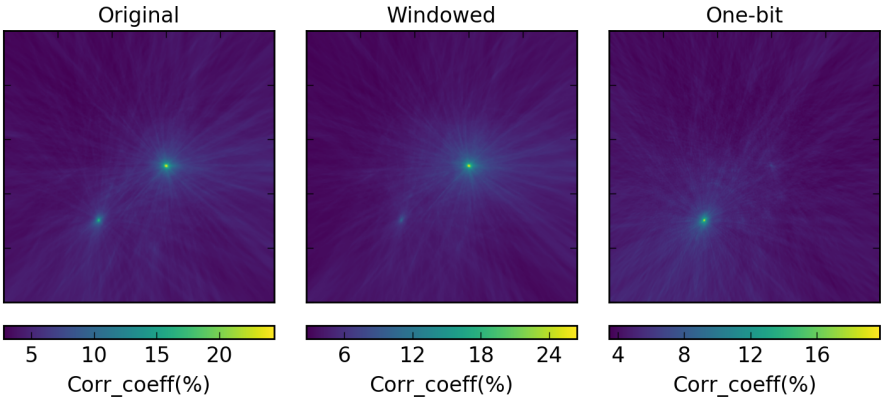

FIGURE 2.5: The effect of cross-correlation window length and one-bit time-domain normalization on the relative output power of the two sources. Left: Window length of 40 ms and no time-domain normalization. Middle: Window length of 15 ms centered around source 1 (microearthquake) and no time-domain normalization. Right: Window length of 40 ms with one-bit normalization of the original recordings. Grid dimensions are the same as in Figures 2.2, 2.3 and 2.4

by temporal decorrelation due to changes in the source-time function (i.e., the persistent source stops).

One-bit time domain normalization [see 68] proves beneficial for enhancing the contribution from persistent sources (e.g., crusher) that have low amplitudes relative to other possible sources (e.g., microearthquakes). As seen in the right panel of Figure 2.5, although the phase of the microearthquake still correlates coherently, its contribution becomes negligible since it only occupies a small fraction of the total window length. For a more detailed discussion on the effect of time-domain normalization, see Chen et al. [69].

Spectral whitening is typically only beneficial when the source of interest is buried by uncorrelated noise as equalization of the spectral amplitudes will enhance its relative contribution [see 70]. Although the sources we are interested in monitoring are typically more energetic than the background wavefield (see

Sections 2.6 and 2.7), we use spectral whitening in all cases for the robustness it provides through reducing the effect of strong contaminant frequencies (e.g., 50-Hz electrical noise and harmonics) commonly encountered in mine seismic systems.

Finally, the frequency range should be chosen to maximize the spatial coherence of the source of interest across the sensor array relative to other potential sources. Although not shown in the synthetic example, this would involve choosing a higher and lower bandpass center frequency to isolate the microearthquake and crusher, respectively.

2.5.2 CCF smoothing to account for uncertainties in the medium

Localization performance depends on the complexity of the medium and how accurately it can be modeled. The simplest model uses a constant velocity, which allows for travel times to be computed analytically from the source-sensor distances assuming straight ray propagation. The use of a constant velocity model typically requires that the signal wavelength be much greater than the length scale of heterogeneities, such that they are effectively ignored. When this is not the case, it can be advantageous to use a heterogeneous velocity model and an associated wave propagator (e.g., ray tracing).

With our eventual goal being to perform real-time monitoring at mining sites, where computer resources are typically limited, the low computational costs associated with a homogeneous velocity model make it our method of choice. Although this has potential to greatly limit spatial resolution, we are more concerned with the general temporal and spatial patterns of seismicity as

opposed to precise locations for individual microearthquakes. For this application, we found the homogeneous velocity model to be a suitable choice.

If the medium has been accurately estimated (i.e., travel times can be accurately calculated), it is possible to beamform using the raw cross-correlated waveforms, which is referred to as coherent time-delay beamforming in matched field processing. In cases where the medium has not been accurately estimated, it becomes necessary to use an absolute-value smoothing process on the cross-correlated waveforms before localization. This is referred to as incoherent beamforming and ensures that coherent peaks overlap correctly in space and do not destructively interfere (due to incorrect phase shifts caused by error in the estimated velocity model).

To account for the significant error introduced by our choice of a homogeneous velocity model, we found it necessary to smooth each cross-correlation prior to computing the functional evaluations. Smoothing can be accomplished in several ways, including taking the envelope computed from the analytic signal or, our method of choice, a sliding window root-mean-square (RMS) according to

$$\mathrm{RMS}(t) = \sqrt{\frac{1}{N} \sum_{i=-N/2}^{N/2} x^2(t+i)} \tag{2.5}$$

where $x(t)$ is the signal and N is the length of the smoothing window. The appropriate setting for N depends on the uncertainty in the velocity model through the potential error in travel-time difference for two rays traveling from the same source to two separate sensors. To ensure coherent peaks correctly overlap, we suggest using a smoothing window length equal to the maximum possible error in travel-time difference. The length of the smoothing window, which reflects the uncertainty in the velocity model, sets the upper bound on location accuracy

and precision.

In general, sensor spacing and array aperture are also important in determining the effectiveness of beamforming techniques. For regularly spaced arrays, resolution is dictated by the minimum inter-sensor spacing through the maximum resolvable frequency (minimum of two samples per wavelength) with aliasing problems becoming an issue when inter-sensor spacing is greater than a few wavelengths. In the case of irregularly spaced arrays, however, it is no longer appropriate to use these wavelength bound limits as a minimum of two samples per wavelength is not guaranteed over the entire array [66]. We did not encounter any strong aliasing effects using this specific beamforming method and refer the reader to Wathelet et al. [71] and [66] for more information on array responses.

2.5.3 Multiple wave types

Another challenge of the InterLoc method is the difficulty in accounting for multiple body wave types propagating at different velocities. For example, when cross-correlating waveforms of a microearthquake with P and S arrivals recorded at two stations A and B, the resulting CCF will have physically meaningful peaks corresponding to $P_A \times P_B$ and $S_A \times S_B$ as well as spurious cross-terms $S_A \times P_B$ and $P_A \times S_B$. In the case of cross-correlating a microearthquake recorded at randomly oriented sensors, the largest amplitude peak in each CCF will most likely correspond to the correlation of the dominant energy phase, which in our case is the direct shear-wave correlation $S_A \times S_B$. Therefore, when locating a source with CCFs containing a mix of contributions from correlating

multiple phase arrivals, using the velocity of the phase with dominant amplitude should prove the most effective approach. Alternatively, isolating the P and S arrivals could be accomplished by rotating tri-axial sensors towards each potential source location.

2.5.4 Localization and triggering

While this technique is well suited to locate sources through an exhaustive grid search (computing a functional evaluation at every potential source location), the computational costs are steep for large search volumes. The requirement to obtain locations in near real-time for certain acoustic applications (e.g. video-conferencing) has led to the development of an application specific search optimization method called stochastic region contraction (SRC) [72, 73]. In summary, given an initial search volume V_0, this method computes the functional evaluation at J random points within the volume and then contracts the volume V_1 to enclose only the N highest values. This process continues iteratively until either a lower limit on the volume is reached, or the highest FE computed within each successive volume stabilizes, indicating that a maximum has been found. This technique has also been extended to multiple simultaneous sources by clustering the initial FEs into high probability regions containing local peaks and then using SRC on each separate region [74]. The number of functional evaluations to compute at each iteration depends on the ratio of the maximum likelihood volume V_{peak} compared to the entire search volume V_0 and the willingness to trade improved performance in exchange for lowering the probability of missing the maximum.

Running the SRC to completion during periods where sources of interest are

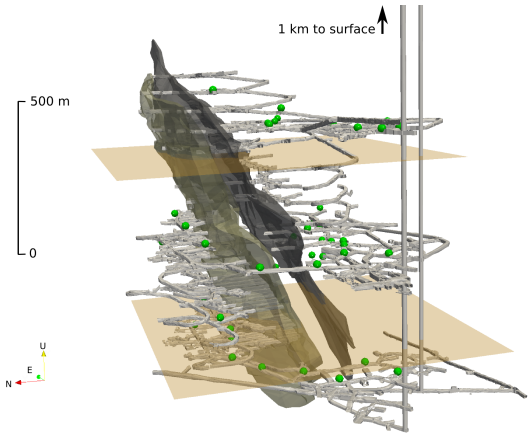

FIGURE 2.6: Mine plans for Nickel Rim South showing tunnels (light gray), ore bodies (dark grays) and sensors (green spheres). The top and bottom planes (both 500×500 m^2) show where the slices for the drilling and microseismic results are taken respectively.

not active is computationally wasteful. To mitigate this, we perform the following steps: after the first iteration, we compute a trigger value $T = P_{max} - P_{min}$ which is the difference between the maximum and minimum FE values; if T is below a predetermined threshold, then there is likely no maximum (or source) to be located and we exit the routine; trigger values that are above the threshold are considered positive triggers and the SRC procedure continues until completion. Practical application of stochastic region contraction will be seen in Section 2.7.1.

2.6 Case study I: Stoping mine

We first validate the location method using continuous seismic data from Nickel Rim South, an active underground stoping mine in Sudbury, Canada. Mine plans and the seismic system, which consists of 28 uniaxial accelerometers and 16 triaxial geophones, can be seen in Figure 2.6. The seismic wavefield at this mine is dominated by drilling, blasting and microearthquakes.

2.6.1 Microearthquake localization

To demonstrate the effectiveness of this method in locating impulsive sources, we look first at a microearthquake of local magnitude -1.5 recorded at 27 nearby channels (mix of uni- and triaxial stations). A window length of 200 ms is used and the raw arrival signals are bandpassed from 20 to 1000 Hz and spectrally whitened (Figure 2.7 left panel). From the pre-processed signals, we compute 344 CCFs (all inter-station channel pairs) and apply a sliding window RMS of length 2.2 ms. We then compute a total of 125 million functional evaluations corresponding to 1 m spacing in a $500 \times 500 \times 500$ m^3 volume. To show the constraint on the focal volume, we plot a slice of the 3D output power through the z-axis at the location of the global maximum in Figure 2.7 (right panel). Next, we one-bit normalize the arrival waveforms and recompute the output power (Figure 2.8). Although the correlation is much weaker, the event location is still clearly identifiable due to the phase coherency of the arrival waveform, which persists through amplitude normalization. Coherency of the phase allows for detection of very weak events, which is not possible with traditional phase picking schemes. This will be explored further in Section 2.7.

2.6.2 Drilling localization

To demonstrate the effectiveness of this method in locating continuous sources, we use a one second period of drilling recorded at 13 nearby channels. The raw arrival signals are bandpass filtered between 500 and 2500 Hz and spectrally whitened to accentuate the drilling (Figure 2.9). The 'smearing' effect of the maximum likelihood volume (or area for 2D slice) is indicative of poor constraint due to lack of sensors behind the ore body at this level. Sensors from

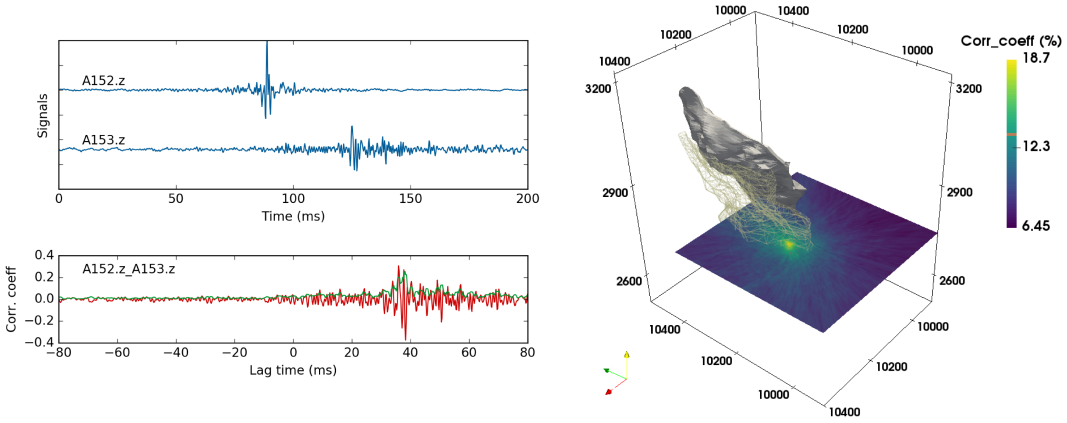

FIGURE 2.7: Left: Example of seismograms for a microearthquake recorded at two sensors (top) and their resulting cross-correlation (bottom). Green solid line in bottom plot is the smoothed signal used in computing the output power. Right: Slice through location of the maximum value of the summed 3D output power computed from 344 CCFs of this event. Although not shown, constraint on focal volume is equal in all directions. Colors represent mean correlation strength in percent.

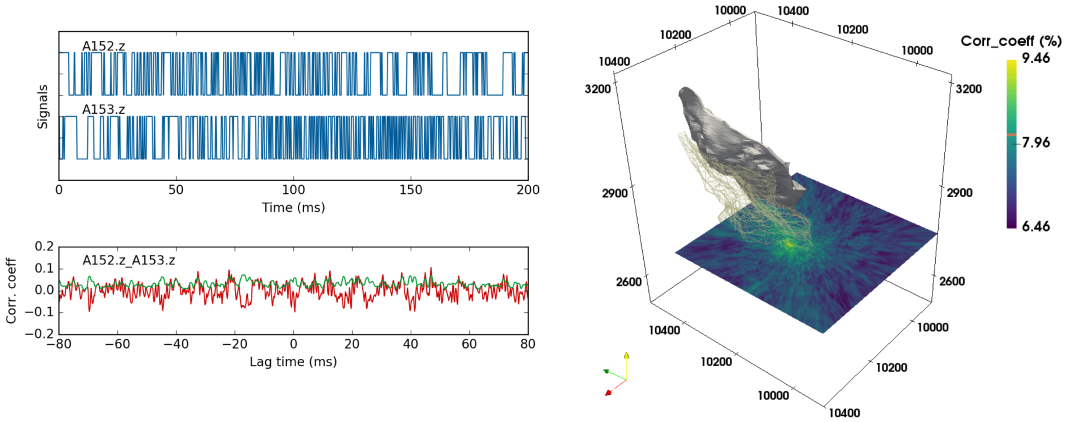

FIGURE 2.8: Same as Figure 2.7 but with waveforms one-bit normalized prior to cross-correlation. Although no obvious correlation peak is discernible for this pair, the result of mapping and summing 344 CCFs still allows for localization of the microearthquake. This is possible due to the phase coherency of the event which persists through amplitude normalization.

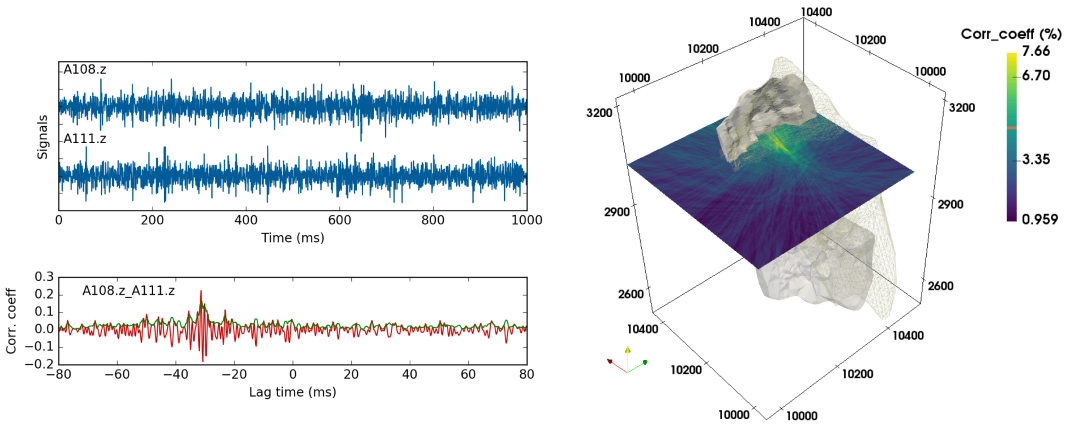

FIGURE 2.9: Same as Figure 2.7 and 2.8 but for a one-second period of active drilling. The smearing of the maximum likelihood volume is caused by poor constraint due to lack of sensors behind the ore body at this level.

lower levels are not used in this case as they provide no additional constraint on source location. This is due to the high-frequency nature of the seismic energy generated by the drilling, which becomes heavily scattered and attenuated by tunnels along the ore body. Nevertheless, using only 13 sensors the InterLoc method successfully identifies and roughly localizes the non-impulsive source of seismic signal in a heavily scattering environment.

2.7 Case study II: Block caving mine

Block caving involves undercutting an ore body and allowing it to progressively collapse under its own weight and is an economical way to mine large volumes of low-grade ore. During this progressive collapse, tracking the cavefront is primarily accomplished by monitoring the location and rate of seismicity, as microearthquakes concentrate in the highly stressed rock immediately above the cavefront fracture zone [75]. Monitoring is important to ensure that the cave

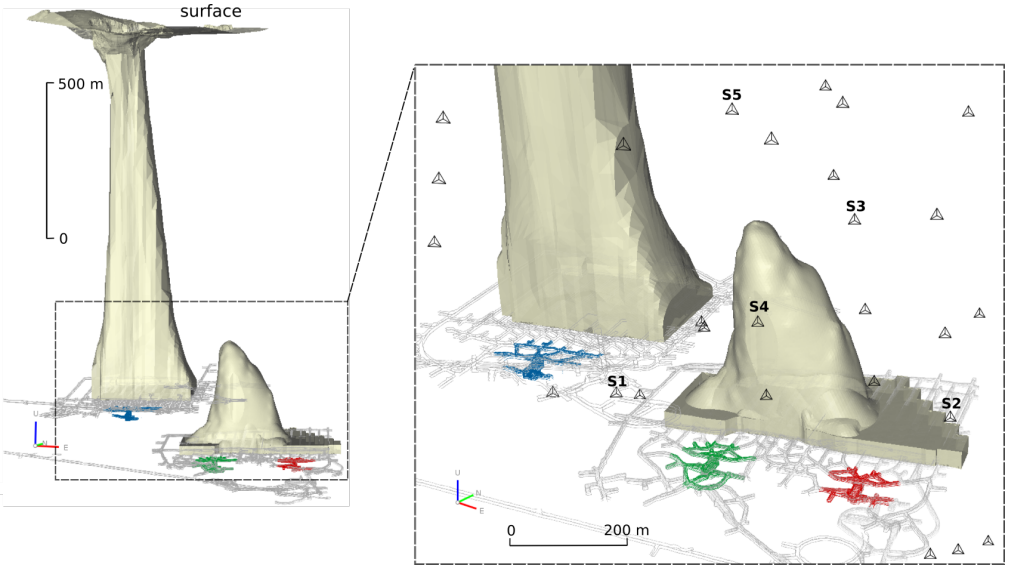

FIGURE 2.10: Mine plans for a block caving mine showing estimated cave shapes in beige, tunnels in gray and ore crushers as blue, green and red respectively. Geophones shown as black triangles with labels on those specifically referred to in the text.

continues to advance and is not drifting away from the ore body. There are also safety implications for identifying periods when the cave has stopped advancing, as continuing to extract material widens the air gap between the cavefront and the yielded material. This creates the potential for powerful and deadly air blasts if a large volume of rock yields at once, effectively jettisoning the air into the connecting tunnels.

This operation (Figure 2.10) consists of an actively propagating block cave from which yielded ore is being removed and crushed. The seismic wavefield at this mine is dominated by three nearly continuously operating ore crushers and hundreds of microearthquakes per day. The seismic system at this mine consists of over 60 tri-axial geophones, however we only use a subset of data from sensors around the cave.

2.7.1 Microearthquake triggering

Here we evaluate the effectiveness of InterLoc in detecting and locating a full day of microearthquakes occurring around the active block cave compared to the traditional STA/LTA trigger and phase-picking scheme used at the mine. Pre-processing parameters include a cross-correlation window length of 500 ms, no time domain normalization, and a bandpass filter with corner frequencies of 200 and 1500 Hz. Time windows are overlapped by 20% to ensure arrivals that span two windows are not missed. Gaps in the continuous recordings at individual sensors due to signal dropout are treated as zeros. To detect and locate microearthquakes within each 500-millisecond window, we use the stochastic region contraction procedure with an initial volume of $600 \times 600 \times 600$ m^3, centered near the top of the block cave. Within each contraction volume $J = 20000$ FEs are computed, sorted, and the next volume is defined around the best $N = 50$. This process is repeated until stabilization of the highest FE value, indicating a maximum has been found. This configuration was determined to be suitable based on repeatedly locating the same microearthquake (located above cave with local magnitude -1.2) for which there is a $\sim$99.7% probability of finding the global maximum.

To avoid calling the SRC locator to completion during time periods with no microearthquakes, we employ the triggering scheme described in Section 2.5.4. An example of how the trigger values vary over the first two hours of the day can be seen in Figure 2.11. Using a threshold of $T = 0.4$ to signify a positive trigger, we detected 585 microearthquakes, which is a great improvement compared to the 98 events (ranging in local magnitude from -2.7 to -0.2) detected by the STA/LTA triggering used at the mine. Locations for all 585 microearthquakes,

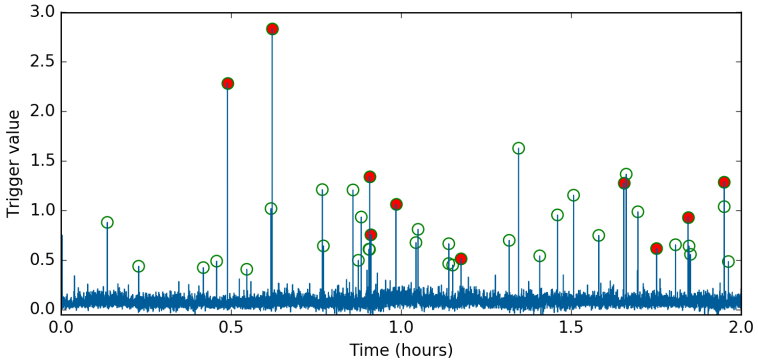

FIGURE 2.11: Plot of trigger values (see Section 2.5.4) over a 2-hour period a using cross-correlation window length of 500 ms with 20% overlap. Values over the threshold of 0.4 (open green circles) are considered detections and subsequently located. Red filled circles indicate events that were also detected by the STA/LTA method currently being used at the mine.

as well as a comparison with the 98 events in the mine catalog can be seen in Figure 2.14. Events in the catalog are located using a probabilistic inversion of manually picked P and S arrival times with uncertainties between 2 and 10 meters. While the locations in the catalog take advantage of the entire seismic system, those computed with InterLoc use only select sensors around the cave. This explains the larger location residuals in the poorly constrained areas further from the cave.

To avoid calling the SRC locator to completion during time periods with no microearthquakes we employ the triggering scheme described in Section 2.5.4. An example of how the trigger values vary over the first two hours of the day can be seen in Figure 2.11. Using a threshold of $T = 0.4$ to signify a positive trigger we detected 585 microearthquakes, which is a great improvement compared to the 98 events (ranging in local magnitude from -2.7 to -0.2) detected by the STA/LTA triggering used at the mine. The threshold value was chosen through a manual review of raw waveforms for dozens of the positive InterLoc

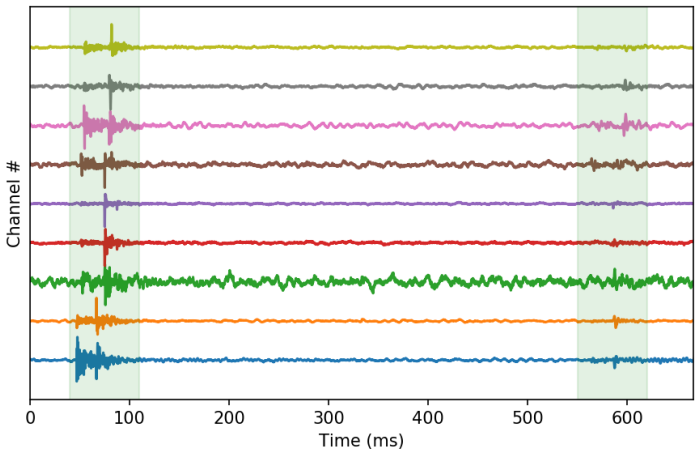

FIGURE 2.12: Raw waveforms for a microseismic event (left shaded area) and an aftershock (right shaded area). InterLoc was able to detect and locate both events with maximum output power of 1.38 and 0.6 respectively.

detections (Figure 2.12). For the detections we reviewed, trigger values above 0.4 were always associated with brief increases in waveform amplitudes. Although not shown here, from the estimated source location it is also possible to shift and stack the absolute-valued waveforms based on the source-station traveltime differences. The time at which the stack has maximum amplitude then corresponds to the most likely origin time.

Uncertainty on the location of each potential event found by InterLoc can be estimated by examining the 3D distributions of output power (Figure 2.13). We are confident that the true location will lie somewhere within the volume encompassing the top 10 percent of output power grid values. For events occuring in the well constrained area above the cavefront this volume gives us a location uncertainty on the order of 10 meters.

Locations for all 585 microearthquakes, as well as a comparison with the 98 events in the mine catalog can be seen in Figure 2.14. Events in the catalog are

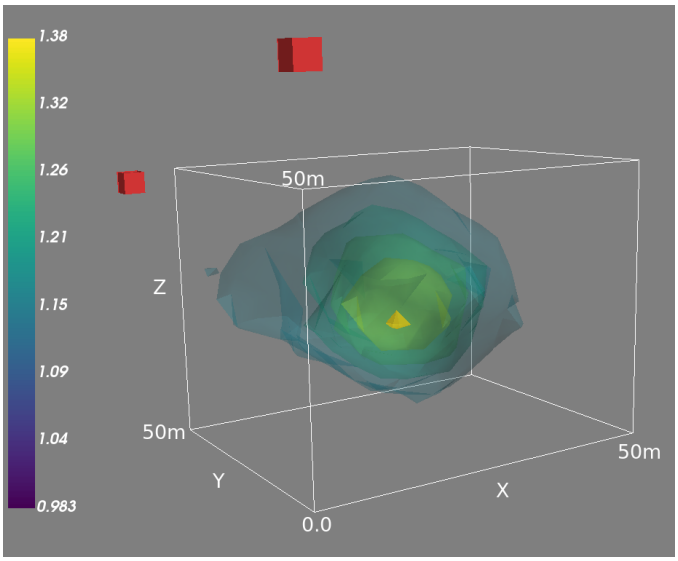

FIGURE 2.13: InterLoc output power (colored contours) with 5m grid spacing for the main microseismic event in Figure 2.12 with stations shown as red cubes. The spatial drop-off in output power moving away from the source provides an idea of the location uncertainty (approximately 5 to 10 meters in this case).

located using a probabilistic inversion of manually picked P and S arrival times with uncertainties between 5 and 15 meters. While the locations in the catalog take advantage of the entire seismic system, those computed with InterLoc use only select sensors around the cave. This explains the larger location residuals in the poorly constrained areas further from the cave.

2.7.2 Monitoring ore crusher activity

To show the potential of interferometry for temporal monitoring of persistent sources, we simultaneously track the activity of all three ore crushers at the block caving mine using a single sensor pair. Although this method does not require directly computing functional evaluations, it requires that the source locations be roughly known so that their contributions can be identified in the

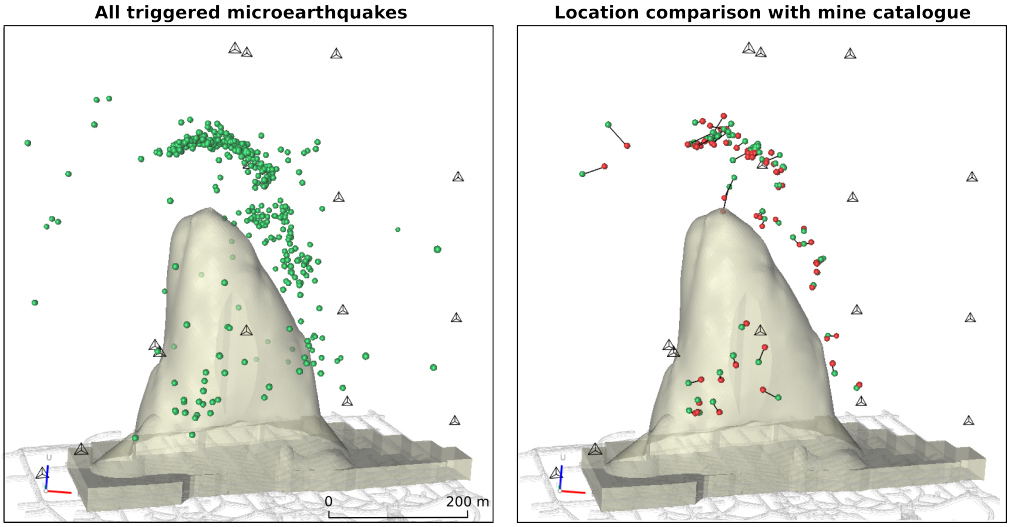

FIGURE 2.14: Left: Locations for one day of microearthquakes as determined by InterLoc using only sensors surrounding this cave (black triangles). Notice how the event distribution is concentrated in the highly-stressed seismogenic zone above the cavefront which allows for inference of cave extent. Right: Comparison of the location of events in the mine catalog (red spheres) with locations of those same events as determined by InterLoc (green spheres).

cross-correlation functions.

The sensor pair S1-S2 (Figure 2.10) is specifically chosen so that the crushers' respective contributions to the pair's CCFs do not overlap. A cross-correlation window length of 10 seconds (with no overlap) is used to strike a good balance between temporal resolution and correlation strength, while bandpass corner frequencies of 40 and 400 Hz help to isolate contributions from the crushers. One-bit normalization is also used to suppress any impulsive contaminating sources such as microearthquakes. Cross-correlation functions are computed for a 35-minute time period (Figure 2.15, middle panel) and then stacked (top panel). Since the crusher locations are known, we can identify lag time windows where each respective $S \times S$ contribution in the CCF should appear (effectively the reverse of InterLoc). The windowed signals of the stack, which represent the

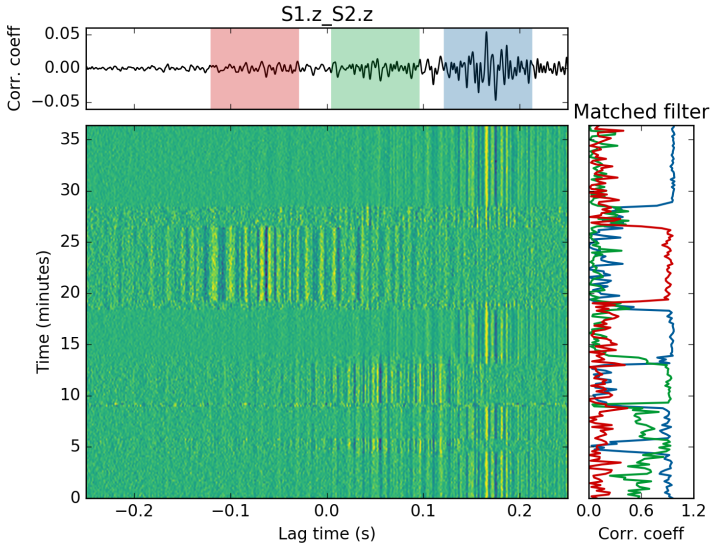

FIGURE 2.15: Individual cross-correlation functions (10 s window length) computed for a single sensor pair over a 35-minute period (mid panel) and stacked (top panel). Since crusher locations are known, we build three templates (color coded for each crusher respectively) from the stack. Right panel: The result of correlating the templates with their respective portions of each individual CCF. These values serve as a proxy for relative crusher activity at any given time.

characteristic waveforms associated with the crushers, are used as the templates (or filters) in a template matching (or matched filter) approach. This method involves correlating the templates with their respective portions of each CCF in a semi-continuous fashion, results for which can be seen in Figure 2.15 (right panel). In interpreting these results we associate active crushers with high correlation values.

The activity of each crusher appears to vary on a timescale of 5 to 10 minutes, which we believe is due to the alternating nature of the feeder and the rock breaker, with the maximum energy emitted during periods of active crushing. The template matching approach allows for identification of periods when both

a single crusher (30-35 minutes), and multiple crushers (0-9 minutes), are active. Monitoring crusher activity in this manner is easy to implement and accounting for any significant temporal changes in the medium or crusher source time functions would be as simple as updating the templates.

2.8 Potential application to ambient noise interferometry

In the absence of persistent sources, ambient noise interferometry can be used to estimate the seismic Green's function between sensor pairs. This technique involves the cross-correlation of a spectrally white and diffuse noise field recorded at sensors A and B to estimate the Green's function G_{AB} of the sensor pair, convolved with the autocorrelation of the noise N, according to:

$$u_{\mathrm{A}}(t) \otimes u_{\mathrm{B}}(t) = [G_{\mathrm{AB}}(t) + G_{\mathrm{AB}}(-t)] * N(t). \tag{2.6}$$

In comparison, by cross-correlating time periods when a persistent stationary source C dominates the wavefield, we are estimating the following function:

$$u_{\mathrm{A}}(t) \otimes u_{\mathrm{B}}(t) = [G_{\mathrm{CA}} * n(t)] \otimes [G_{\mathrm{CB}} * n(t)] \tag{2.7}$$

where $n(t)$ is the source-time function of the persistent source. This can be described as the cross-correlation of the two source-sensor Green's functions convolved with the source time function of the persistent source. Although both

functions (eq. 2.6 and 2.7) contain information on the medium, they are qualitatively different and must therefore be measured differently. By blindly cross-correlating and stacking data when persistent sources often dominate the wavefield, we are effectively combining these qualitatively different functions and then incorrectly interpreting the final result as the estimated Greens function for the sensor pair (eq. 2.6). For a correct interpretation, both the locations and nature of seismic sources need to be known so that their contributions to the final correlation function can be identified and understood, as in Section 2.7.2.

Alternatively, instead of blindly summing all cross-correlations, we can use InterLoc to assess wavefield conditions at each time period and only stack correlations of relatively diffuse periods for a closer estimate of eq. 2.6. This involves evaluating the orientation of each sensor pair with respect to the energy distribution of the seismic wavefield for short successive time periods, and only time periods that are favorable are used to construct the cross-correlation functions. In this case, we identify favorable conditions as when either: 1) no strong sources are present and the wavefield is relatively diffuse; or 2) for a given sensor pair, strong sources are located in, or scattered off stationary phase locations (the conical areas behind each sensor pointing toward the other, see Roux and Kuperman [37]).

Although not shown here, we found that this form of selective stacking produces very similar results to the selective method based on the signal-to-noise ratio used by Olivier et al. [40] but without the need to define an expected arrival time window and risk artificially constraining the signal. While both of these selective stacking methods are effective, they require that sufficient suitable periods exist to allow for convergence to the estimated Green's function in

a reasonable amount of time. In environments where at least one strong source is always active, as with the ore crushers at the caving mine, these periods will be very rare for the majority of sensor pairs. Moreover, selective stacking in this case appears counter-intuitive in the sense that we are trying to remove stable sources (crushers) to create stable sources (from sensors) through ambient noise interferometry.

2.9 Temporal monitoring with stable source interferometry

In this section we demonstrate how stable persistent sources, seen as contaminants in both microearthquake and ambient noise monitoring, can be used to monitor changes in the rockmass with high temporal resolution. This method follows from Section 2.7.2 and takes advantage of the stable waveforms created by cross-correlating time periods where one or more crushers are active. To illustrate this concept we show the potential of using the ore-crushers to monitor an advancing block cave.

As seen in the last section, by cross-correlating and stacking time periods where a single ore crusher C dominates the wavefield, we are effectively estimating eq. 2.7. In the situation where G_{CA} and $s_C(t)$ remain stable, changes in $u_A(t) \otimes u_B(t)$ can be attributed to changes in G_{CB}. Ignoring scattering and reflections, this Green's function is primarily determined by the direct arrivals, which are a coupling between the geometry of the least-time ray path (between C and B) and the medium along this path (described by a sensitivity kernel). Therefore, if this ray path passes through or near areas where we expect changes in

the medium, we can monitor these changes through $u_A(t) \otimes u_B(t)$.

To demonstrate this concept, we compare CCFs computed 66 days apart, a period during which the block cave is estimated to have propagated upwards by $\sim$180 m (Figure 2.16 right panel). To show the potential temporal resolution that can be achieved, we use only one minute of data from each day (during which the blue crusher is active) to compute the cross-correlations. Cross-correlation functions were computed for two different sensor pairs: (1) $u_{S1} \otimes u_{S2}$ which is used as a control; and (2) $u_{S1} \otimes u_{S3}$, from which we hope to monitor changes. The control function is used to show that $G_{C,S1}$ remains relatively stable and therefore any changes in $u_{S1} \otimes u_{S3}$ are caused by changes in $G_{C,S3}$. We are specifically interested in changes along the ray path that connects the blue crusher with sensor S3 and passes very close to the propagating cavefront.

Results for this temporal comparison of CCF waveforms can be seen in Figure 2.16 with the control pair (top panel) remaining nearly identical over the two-month period. On the other hand, comparing the $u_{S1} \otimes u_{S3}$ waveforms (bottom panel) we can see both qualitative differences as well as a time shift of $\sim$2.2 ms. We interpret the time shift, measured by cross-correlating the two waveforms and using the lag time corresponding to the maximum amplitude peak, as the additional travel time incurred by the direct S-wave having to now partially circumvent the cave. This additional travel time is equivalent to $\sim$7 m of additional propagation distance at a velocity of 3200 m/s, which agrees with the changes in cave geometry with respect to this raypath.

The main advantage of this technique over ambient noise interferometry is the high temporal resolution afforded by strong sources, as opposed to relying on the weak multiply scattered seismic wavefield. Future work will involve

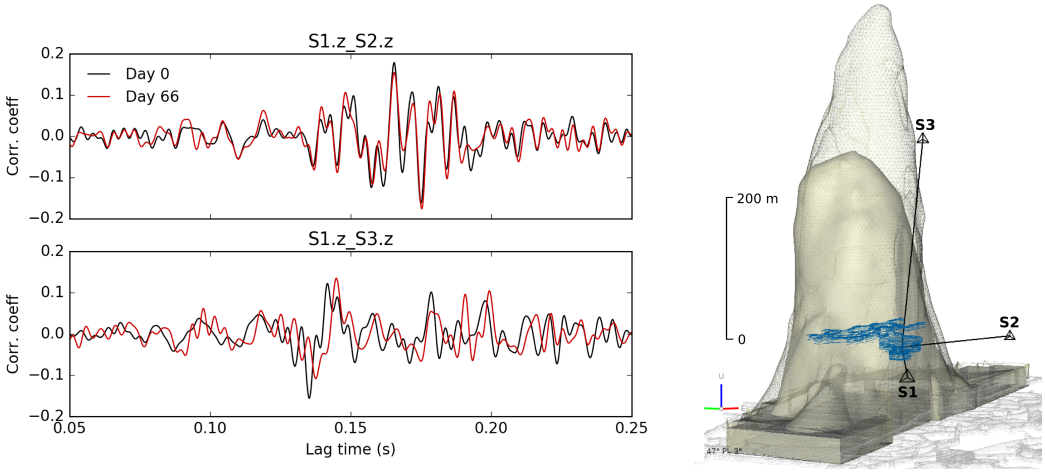

FIGURE 2.16: Cross-correlation functions for two sensor pairs computed 66 days apart, during which the block cave has propagated upwards (faded beige). Each CCF is computed from one minute of data during which the blue crusher is dominant. The CCF in the top panel is used as the control to show that there is no change along the raypath connecting the crusher and sensor S2. The CCF in the bottom panel has shifted and changed qualitatively at certain lag times due to changes in the medium along the ray path connecting the crusher and sensor S3. In this case the propagating block cave has delayed the maximum amplitude arrival by about 2 ms.

monitoring these waveforms (computed for multiple sensor pairs) in semi-continuous time, to improve spatio-temporal constraint on the propagating cave. Hopefully this method will be considered when designing mine seismic systems by ensuring some crusher-sensor ray paths sample areas of interest.

2.10 Conclusions

Detection and location of seismic sources is still predominantly accomplished using triggering and phase-picking methods. Originally developed with the impulsive nature of earthquake rupture in mind, these methods fail under conditions when arrival times cannot be accurately picked; typically when sources are weak, persistent or simultaneously active. The interference of arrival waveforms, accomplished through cross-correlation, provides a robust alternative by removing the need to identify arrival phases. This is a key component in the interferometric locator, a proven and popular localization method which utilizes spectrally whitened cross-correlations in a beamforming-like approach. The success of this technique lies in the robustness of cross-correlations, the insensitivity to environmental conditions exhibited by spectral whitening, and the localization advantages of a steered beamformer. Practical considerations for this technique include pre-processing of the signals to isolate sources of interest, calculating travel times based on the velocity of the dominant amplitude phase and smoothing of the cross-correlation functions prior to localization to account for uncertainties in the medium. While an exhaustive grid search for potential source locations is possible, we recommend implementing the stochastic region contraction procedure for its computational efficiency and simple parameterization.

The robustness of the InterLoc method was demonstrated through the detection, location and monitoring of a variety of seismic sources with three different datasets. The synthetic dataset showed the ability of the method in locating two simultaneous sources under different processing parameters, while data from two active underground mines was used to effectively monitor both impulsive and persistent sources. While InterLoc maps cross-correlation functions into space, there is also value in the reverse process, which is mapping a known source location to its respective lag time in a cross-correlation function. Using this method, we were able to simultaneously monitor the activity of all three ore crushers at a block caving mine using cross-correlations from a single sensor pair in a template matching approach. Information on source locations and activity can also be integrated with ambient noise interferometry to improve estimates of seismic Green's functions under temporally variable and anisotropic wavefield conditions. This involves creating a selective stacking filter that evaluates the orientation of each sensor pair with respect to the energy distribution of the seismic wavefield for short successive time periods, and only time periods that are favorable are used to estimate the final Green's functions.

Additionally, we demonstrated how cross-correlation functions of strong persistent sources (ore crushers), typically seen as contaminants in both microearthquake and ambient noise monitoring, can be used to monitor changes in the medium between source and sensors. The main advantage of this technique over ambient noise interferometry is the high temporal resolution afforded by strong sources, as opposed to relying on the weak multiply scattered field.

Chapter 3

Seismic interferometry using persistent noise sources for temporal subsurface monitoring

Philippe Dales[1], Pascal Audet[1], Gerrit Olivier[2],

[1]Department of Earth and Environmental Sciences, University of Ottawa

[2]Institute of Mine Seismology, Hobart, Tasmania

A version of this chapter has been published. P. Dales, P. Audet, and G. Olivier. Seismic interferometry using persistent noise sources for temporal subsurface monitoring. *Geophysical Research Letters*, 44, 10,862-10,870, 2017.

3.1 Summary

In passive source seismology, seismic interferometry typically refers to the cross-correlation of ambient noise to construct an estimate of the Green's function between sensors. The presence of persistent natural and/or anthropogenic sources can bias or prevent the retrieval of these estimated Green's functions. Here we show how these strong persistent sources can be used to measure small changes in the medium between a source and either (or both) source-sensor pairs. The method relies on localizing the sources and using this information to identify and select cross-correlation functions for each source of interest. We illustrate this method by monitoring growth of a block cave at an underground mine using three nearly continuously operating ore-crushers that dominate the wavefield. This technique should work equally well in natural environments using sources such as volcanic tremor, hydrothermal bubble cavitation and microseisms.

3.2 Introduction

3.2.1 Seismic Interferometry

First proposed by Claerbout [35], seismic interferometry typically refers to the cross-correlation and summation of seismograms to create virtual events, or to the deconvolution of a controlled active source in seismic exploration projects. It has since been demonstrated that the cross-correlation of ambient seismic noise can be used to construct estimates of the Green's function between sensor pairs, effectively turning each sensor into a virtual source [36, 37, 38, 39] and allowing for very sensitive monitoring of temporal velocity changes in the medium between sensor pairs [41, 42]. One of the primary limitations of this method is the reliance on either a fully diffuse wavefield (i.e., equipartition of modes) or a homogeneous distribution of spectrally white noise sources [43, 44], although these conditions can be relaxed slightly in the presence of scatterers that act as secondary sources [45].

Changes in the noise source distribution induce greater errors in the reconstruction of the direct waves in the seismic Green's function than in the coda [76, 77]. As a result, most studies using ambient noise cross-correlation to measure changes in seismic velocity have been done in the coda waves of the reconstructed Green's function [e.g., 78, 79, 80]. However, when the sensor distribution is sparse, it may be useful to use the direct waves to get an estimate of the location of the measured changes. Also, if large changes in medium are expected, the coda of the cross-correlation functions (CCFs) may become incoherent over time and prohibit its use to measure changes in the medium.

Mathematically, the cross-correlation ($\otimes$) of ground velocity in a spectrally

white and diffuse noise field $u(t)$ recorded at sensors A and B estimates the Green's function $G_{AB}(t)$ of the sensor pair, convolved ($*$) with the autocorrelation of the noise $N(t)$, according to:

$$u_A(t) \otimes u_B(t) = [G_{AB}(t) + G_{AB}(-t)] * N(t). \tag{3.1}$$

In environments such as underground mines, where few strong sources produce anisotropic and directional wavefields, conditions are generally not suitable to estimate seismic Green's functions [40]. For example, by cross-correlating time periods when a single persistent stationary source C dominates the wavefield, we are estimating the following function:

$$u_A(t) \otimes u_B(t) = [G_{CA} * n(t)] \otimes [G_{CB} * n(t)] \tag{3.2}$$

where $n(t)$ is the source-time function of the persistent source. This equation can be described as the cross-correlation of the Green's functions for the two source-sensor pairs convolved with the source-time function of the persistent source. In the case where G_{CA} and $n(t)$ remain stable, any change in $u_A(t) \otimes u_B(t)$ must be due to changes in G_{CB}. The seismic Green's function G_{CB} is primarily influenced by the direct arrivals, which are a coupling between the geometry of the least-time ray path (between source C and sensor B) and the medium along this path (described by a sensitivity kernel). Therefore, if this ray path passes through or near volumes where we expect changes in the medium, we can monitor these changes through $u_A(t) \otimes u_B(t)$ [20].

Although the use of active sources to perform temporal monitoring is not a novel technique [e.g. 81]), here we are dealing with multiple persistent and

uncontrolled sources. We define an uncontrolled seismic source as a source for which we cannot control the location and/or source-time function. This problem is frequently encountered in applications of ambient noise interferometry where few persistent sources often dominate the CCFs, resulting in arrivals at non-physical lag times (with respect to inter-station propagating seismic waves). We would like to highlight that, once located, these typically contaminating sources can be exploited to perform temporal monitoring. Using uncontrolled sources to perform temporal monitoring has not been used routinely in seismology but equivalent methods have been used for many years in radio astronomy [e.g. 82]. Very-long-baseline interferometry (VLBI) involves the detection of an uncontrolled astronomical source (such as a quasar) in multiple radio telescopes on earth. These signals are then cross-correlated between different radio telescope pairs. By looking at changes in the arrival times in the cross-correlation function, the distance between the radio telescopes can be measured to within millimeters to show the movement of tectonic plates. In our case we use cross-correlations of time periods where an ore crusher is active to monitor the growth of a block cave.

3.2.2 Block caving mines

Block caving (see Fig. 3.1 left panel) involves undercutting an ore body and allowing it to progressively collapse under its own weight and is an economical way to mine large volumes of low-grade ore [for more details, see 83]. To enable the collapse (which can take up to several years), trucks must continuously remove the broken ore from the extraction level to nearby conveyor belts which

feed the ore crushers. Monitoring the progressing cave has important implications for both production and safety but limited access to the cave front makes this a difficult task. In terms of production, tracking the cave front is important to ensure that the cave continues to advance on schedule and is not drifting away from the target ore body. In terms of safety, it is important to identify periods when the cave has stopped advancing, as continuing to extract material widens the air gap between the cave front and the yielded material. This creates the potential for a powerful and deadly air blast if a large volume of rock yields at once and compresses air into any connecting tunnels.

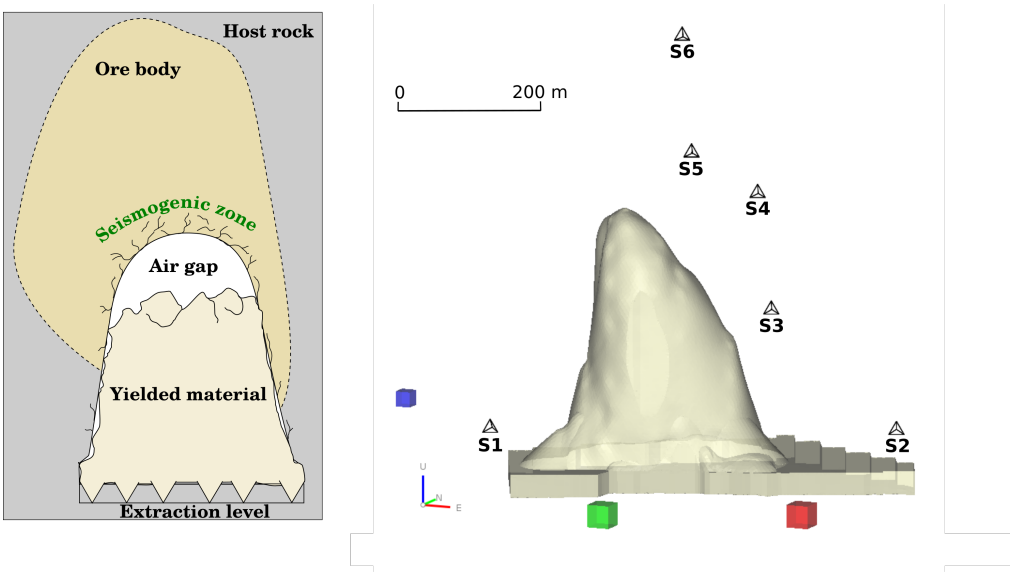

FIGURE 3.1: Left: Cartoon example of a block cave. After initial blasting the cave front should naturally propagate to the surface as material is drawn from below. Microearthquakes concentrate in the highly stressed rock above the cave known as the seismogenic zone. Right: Mine plans for a block caving mine showing estimated cave shape in beige and ore crushers as blue, green and red respectively. Geophones shown as black triangles with respective sensor names as labels.

During this progressive collapse, tracking of the cave front is primarily accomplished using a combination of boreholes (drilled to intersect the cave) and

passive microseismic monitoring. Although boreholes allow for direct access to the cave front, drilling is expensive and periodically lowering instrumentation (e.g., cameras) down the holes is labor intensive. In contrast, microseismic monitoring is relatively cheap and easily automated. This involves using information on the location and rate of seismicity, as microearthquakes typically concentrate in the stressed rock immediately above the cave-front fracture zone [18, 75, 20]. Drawbacks of microseismic monitoring are that cave growth can still occur without generating any detectable events and there is little constraint on lateral growth as few events occur around the sides of the cave.

Although existing cave-tracking methods are unlikely to be replaced, there is a need for new complementary and cost-effective monitoring techniques. Our proposed technique has the advantage of using existing mine infrastructure and being easily automated.

3.3 Data and methods

Our dataset consists of 40 days of continuous seismic recordings from an operational block cave mine for which the estimated cave outline can be seen in Figure 3.1 (right panel). The seismic wavefield at this mine is dominated by three nearly continuously operating ore crushers (at least one is active at all times) and hundreds of microearthquakes per day. An example of the signal generated by an ore crusher and recorded at a nearby sensor can be seen in Fig.3.2. Operation of an ore crusher alternates between a loading phase, where ore from the conveyor belt fills the gyratory crusher, and an active phase where the ore is ground. Each of these phases typically lasts between 2 to 10 minutes with maximum energy emitted during the active crushing phase where the source-time

function is determined by the nature of the material being crushed. Although the locations of the ore crushers are known and fixed, in practice (i.e., as seismologists not wishing to interfere with production) we do not control their locations or operational scheduling.

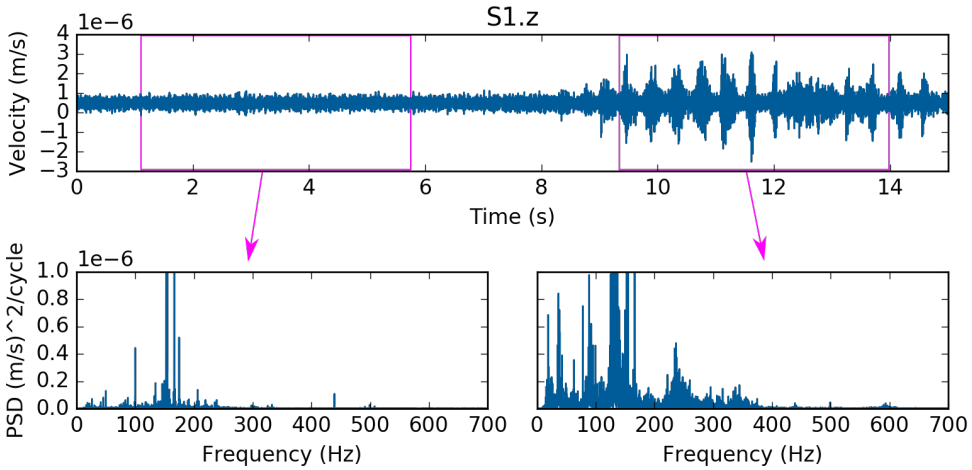

FIGURE 3.2: Top: Typical signal recorded at the sensor nearest the blue ore-crusher for a period during which the crusher begins actively crushing ore. Bottom: Power spectral density of the signal for the two highlighted time periods.

The seismic system at this mine consists of over 60 tri-axial geophones; however, to illustrate our technique, we use only vertical component data from a subset of six sensors. The sensor nearest the blue ore crusher (S1) serves as the reference station (as we expect minimal change in the medium between this sensor and the ore crusher) whose signal is cross-correlated with recordings from the five other sensors (S2 to S6) surrounding the cave.

The goal of the data pre-processing is to maximize the contribution the persistent sources make to each cross-correlation function. To achieve this, the raw recordings are bandpass filtered between 50 and 500 Hz, where the crusher is most energetic, spectrally whitened to reduce the effect of electrical noise and

one-bit time domain normalized to remove the contribution from microearthquakes [see 68]. A cross correlation window length of ten seconds is used with the resulting waveforms selectively stacked (based on crusher activity) into ten-minute long blocks. The result is 5760 CCFs for each sensor pair over the 40-day period.

When the persistent sources operate intermittently in time (such as the ore crushers), selective stacking of the individual CCFs can greatly simplify the process of interpreting and making measurements from the final stacked CCFs through isolation of the contribution from a specific source. Selective stacking is accomplished using a template matching approach where the templates are created from a cross-correlation function for a single sensor pair. Since the crusher locations are known, we can identify lag-time windows where each respective $S \times S$ contribution in the template CCF should appear based on the difference between the two crusher-sensor travel times. Note that in cases where the source distribution is unknown, it can easily be determined by beamforming using the CCFs themselves [see 20]. These windowed signals, which represent the characteristic waveforms for each crusher, are used as the templates and are then correlated with their respective portions of each CCF in a semi-continuous fashion, results for which can be seen in Figure 3.3 (right panel). We associate high correlation value with active crushing to selectively stack periods where each crusher is active. To demonstrate the cavefront tracking technique we restrict ourselves to only using CCFs from periods when the blue crusher is active.

The next step is to measure temporal changes in the CCFs for each sensor pair over the 40-day period. We expect crusher-sensor travel times to increase for those rays that are nearby or that intersect the growing cave. Travel-time

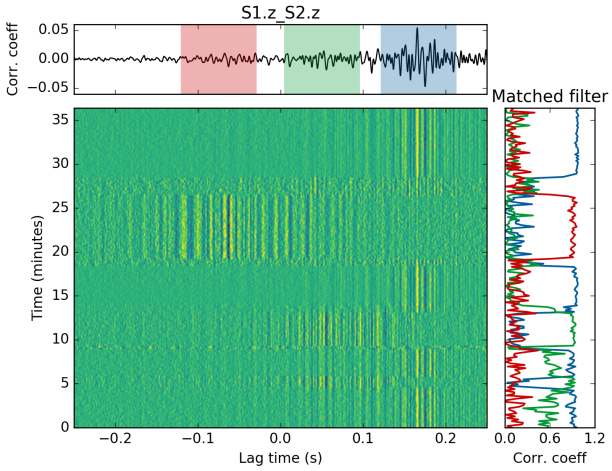

FIGURE 3.3: Individual cross-correlation functions (10 s window length) computed for a single sensor pair over a 35-minute period (mid panel) and stacked (top panel). Since crusher locations are known, we build three templates (color coded for each crusher respectively) from the stack. Right panel: The result of correlating the templates with their respective portions of each individual CCF. These values serve as a proxy for relative crusher activity at any given time. Reproduced from [20].

changes are measured using a simple marching method, which follows an initially selected local minimum or maximum in the CCF over time. We found this type of method to be robust (compared to correlation-based methods) when dealing with waveforms that undergo strong qualitative changes over time. In this monitoring case, where we are only concerned with a targeted volume, it would be inappropriate to use more sensitive measurement techniques (e.g., MWCS [84, 42]), which measure changes in bulk properties by exploiting the multiply scattered coda. In addition, we do not require sub-sample precision since the travel-time changes caused by cave growth should be on the order of several percent. Nevertheless, there is still valuable information on cave growth contained in the coda, although it is more difficult to extract and interpret. For example, qualitative changes (e.g., breaks or new branches) in the coda would indicate that the cave has interfered with a certain multiply scattered path. With enough of these measurements it should be possible to more precisely locate where changes have occurred in the rock mass [see 85].

3.4 Results and discussion

As expected, we see no significant changes in the waveform of the reference pair (Fig. 3.4, left panel) as the direct crusher-sensor ray path should not be affected due to its distance from the cave. In comparison, the CCF for the sensor pair S1-S5 undergoes significant qualitative and quantitative changes over time (Fig. 3.4 right panel). Zooming in on the $S \times S$ portion of the waveform for this sensor pair (Fig. 3.5) reveals a clear moveout of the signal which we interpret as the additional travel time incurred by the direct S-wave having to now partially circumvent the cave. This additional travel time is equivalent to $\sim$40 m

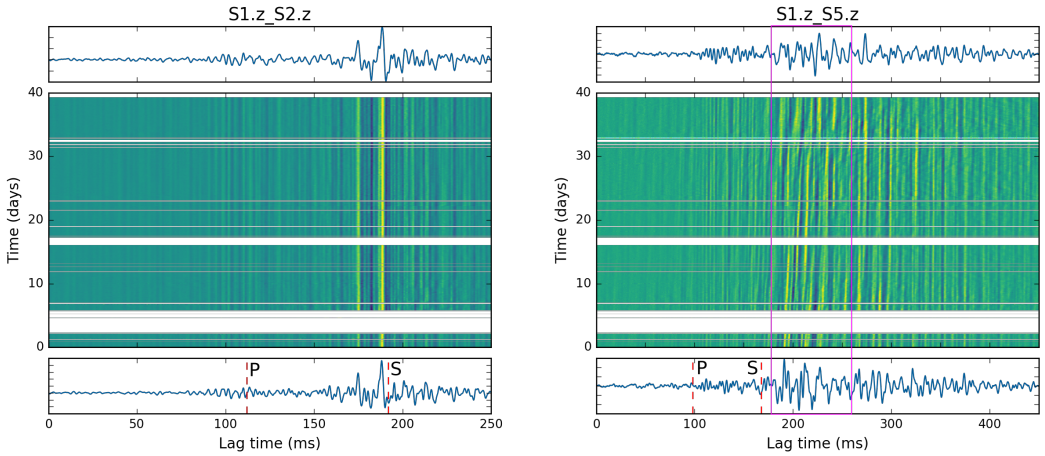

FIGURE 3.4: Comparing CCFs for two sensor pairs (S1-S2 and S1-S5) over 40 days. For both pairs the CCFs have been selectively stacked to isolate periods where the blue crusher is active. Dashed lines indicate where we expect to see the P- and S-wave arrivals assuming straight ray paths and homogeneous velocities of 5600 and 3200 m/s, respectively. Note that only positive lag times are shown here as we do no expect any arrivals at negative lag times given these source-sensor geometries. Pink box shows lag-time window where we make measurements in Figure 3.5.

of additional propagation distance at a velocity of 3200 m/s, consistent with the estimated changes in cave geometry with respect to this ray path.

The same measurements for all crusher-sensor ray paths over the 40-day period are shown in Figure 3.6. The interpretation of these changes is intuitive when looking at the ray paths with respect to the cave geometry. Since the purple ray path already intersects the cave on day 0, it exhibits travel-time changes throughout the whole 40-day period. Comparing this with the blue ray path, significant travel-time increases only start to be seen around day 20, the time at which the cave has grown high enough to begin affecting the ray. Finally, the small steady increase in the orange and green path lengths are most likely caused by lateral cave growth. Although we interpret the travel-time increase as purely path length increases, it could also be partly due to a decrease in the

bulk velocity of the rock (due to fracturing or a decrease in stress as shown in Olivier et al. [19] and Olivier and Brenguier [86]).

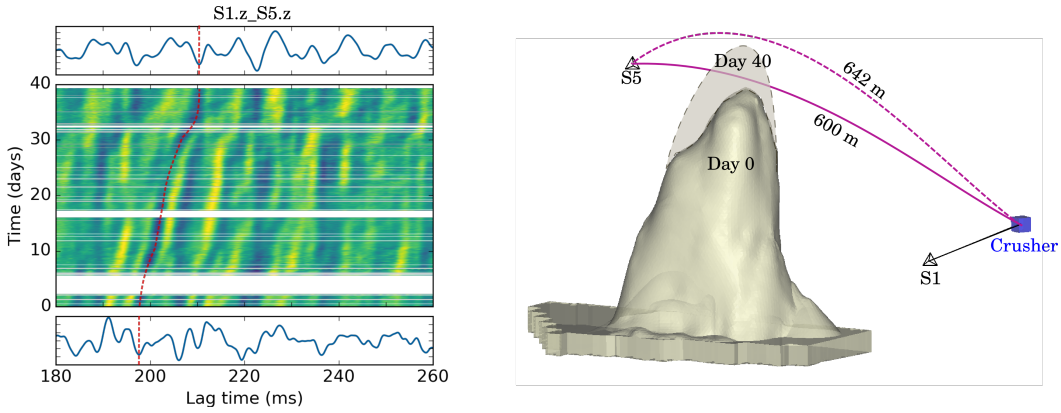

FIGURE 3.5: Left: Cross-correlations for the S1-S5 sensor pair over 40 days zoomed in on the main wavepacket (outlined in Fig. 3.4). We follow a minimum in the CCF using a simple marching method (dashed line) to obtain the travel time change. Right: Cartoon example comparing estimated original ray path (solid line) with new ray path (dashed line) assuming additional travel time is due to path length increase.

In addition to the quantitative changes, the cross-correlated waveforms also exhibit interesting qualitative changes. One example is a splitting (or branching) effect of a peak in the CCF as the cave grows directly through the associated crusher-sensor ray path (Fig. 3.7 near day 27). We believe this effect is due to the waves, which previously traveled directly between crusher and sensor, now propagating around both sides of the cave with slightly different travel times. In general, these qualitative changes prove difficult to interpret and will require a detailed comparison with synthetics. Once we can confidently interpret our measurements, the next step will be to estimate the cave shape in near real-time.

Although we have demonstrated this technique in an industrial environment, it should extend to any environment where persistent sources exist. For example, perhaps volcanic tremor [64, 65] could be used to detect expansion

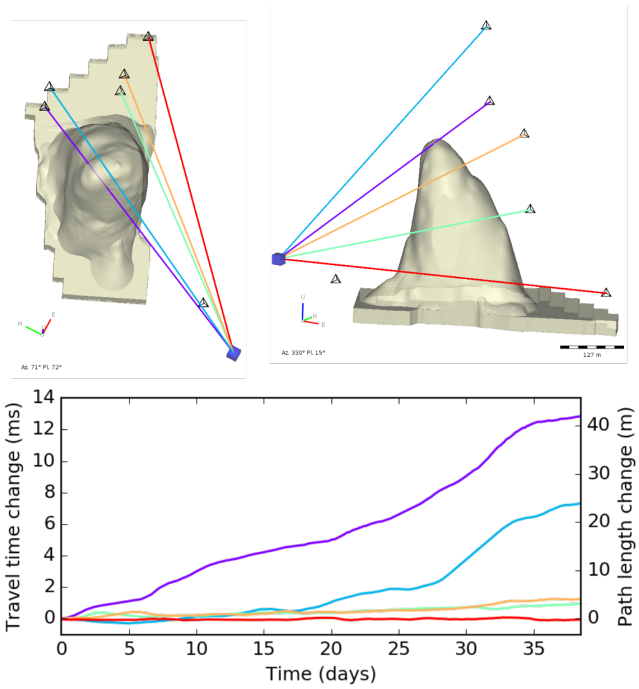

FIGURE 3.6: Top: Geometry of the crusher-sensor ray paths with respect to the cave. Bottom: Travel-time changes measured along each respective path. Secondary y-axis shows path length change assuming additional travel time is purely due to path length increase.

of the volcanic edifice, an eruption pre-cursor. Other potential natural seismic sources include bubble cavitation in hydrothermal systems [87] as well as microseisms and storms [53, 88, 89].

This technique is best suited for sources with either fixed locations (e.g., crushers) or stable time-averaged locations (e.g., hydrothermal bubble cavitation will occur randomly but within a fixed volume) but could also be extended to non-stationary sources (e.g., migrating storms) as long as they can be well localized at each time step. For example, any changes in travel-time difference that deviate from theoretical changes (calculated from the change in source position) would indicate a changing medium. The cross-correlation window length in

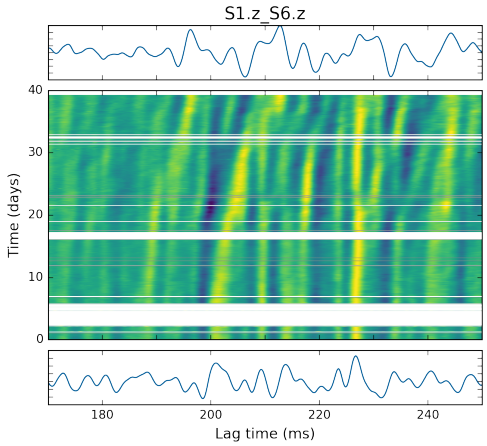

FIGURE 3.7: CCFs for sensor pair S1-S6 showing interesting branching behavior as cave grows through the blue ray path. This effect could be due to the waves now propagating around both sides of the cave with slightly different travel times.

this case becomes very important and will depend on the source velocity. Care must also be taken in interpreting measurements as the source-sensor ray paths would be continually sampling a different medium. In summary, for a moving source there will be many trade-offs and optimal processing will depend on the specific case (e.g., source-sensor geometries, source velocity, source strength, desired measurement sensitivity, etc.).

3.5 Conclusion

We have shown the potential of using cross-correlations of time periods where multiple persistent sources (ore crushers) are active to monitor temporal changes in the rock mass (tracking a propagating block cave). To isolate the contribution from a single crusher (and facilitate interpretation), a template matching

approach was used to selectively stack CCFs based on relative crusher activity. From the resulting CCFs, a simple marching method was used to measure travel-time changes in these waveforms over the 40-day period. We attribute these travel-time changes to the additional path length incurred by the crusher-sensor ray paths having to circumvent the growing cave. Although we have shown an example from an industrial environment, this technique should extend equally well to persistent natural sources such as volcanic tremor, hydrothermal bubble cavitation and microseisms.

Chapter 4

Dense array processing for seismic source localization

Philippe Dales[1], Gerrit Olivier[2], Pascal Audet[1],

[1]Department of Earth and Environmental Sciences, University of Ottawa

[2]Institute of Mine Seismology, Hobart, Tasmania

4.1 Summary

As dense arrays become increasingly popular, there is a need for effective ways to process the large datasets they produce to detect and locate microseismic events. We begin with an overview of recent work in this domain and then describe our processing workflow, which involves: (1) reducing the data volume by stacking without time shift of spatially close stations; (2) dividing the resulting stacks into sub-arrays (or patches) to exploit local similarity of arrival waveforms and reduce potential travel-time errors; (3) beamforming with spectrally whitened waveforms; and (4) aggregating results for all patches to infer detections. To illustrate these steps we use a synthetic example where the location of a microseismic event buried in uncorrelated noise is successfully retrieved. Next we process a real dataset resulting from a 10,050 node survey that was deployed to evaluate the suitability of a 3×3 km^2 piece of land for carbon sequestration. To validate our processing, we locate vibroseis sweeps and vehicles traveling along nearby highways. Next, we show how acoustic waves generated from nearby pumping stations create artifacts in the beamformer output and how this can be minimized when searching for microseismic events. Based on properties of the dataset, we establish a detection threshold of moment magnitude -0.5 and above. While we cannot dismiss the possibility of small microseismic events below M_w-0.5, we detect no events larger than this. Therefore this is likely a good repository for carbon storage however additional work is needed to further assess the possible presence of smaller event activity.

4.2 Introduction

Cheaper electronics and wireless technology have led to the increasing popularity of large-N (where N refers to number of nodes) seismic arrays that record continuous ground motion. For active source petroleum surveys, these nodal arrays are typically deployed from a few days to weeks, depending on how long it takes for the sources (e.g., vibroseis or explosives) to be shot. Instead of recording only time periods when the sources are firing, it is becoming increasingly common to keep and process the passive data to extract any additional information about the subsurface. One popular example is the 5,200 node deployment in Long Beach, California, where the passive recordings have been used to perform ambient noise surface wave tomography [27, 28], microseismic event detection [90, 91] and traffic monitoring [29].

This paper focuses on the methodology for detection and localization of seismic sources using large surface arrays of one-component sensors (i.e., geophones). While we would like the ability to locate any type of seismic source, our primary interest is in microseismic events that are typically characterized by shear failure along a single fault plane [see 92, 93]. Although borehole stations are favorable for recording body-wave arrivals generated by microseismic events, surface stations are more common due to the high cost of drilling and the temporary nature of most deployments.

The three basic components of surface array data processing methods are waveform pre-processing, time shifting and stacking (i.e., summing or combining). The purpose of time shifting is to align arrival waveforms recorded at each station in the array with respect to a single source location. Time shifts are calculated using estimated travel times between a source and station locations.

Once aligned, stacking is used to increase the signal-to-noise ratio (SNR), i.e., to enhance any weak but coherent energy originating at that source location and recorded by the array. This process of aligning and stacking waveforms for each point in space is referred to as beamforming, migration or back-projection imaging [see 94]. Since this process is necessary for source localization, we refer to methods that do not apply time shifts prior to stacking as 'detection only'.

Detection-only methods [see 30, 90] are appropriate when arrival waveforms for each station are already sufficiently aligned to constructively interfere when summed. This condition is met when the array aperture is much smaller than the apparent wavelength $\lambda_a = \lambda / \sin\theta$ where θ is the angle between the incoming wavefront and the surface. In the case of a planar wavefront coming directly from below (e.g., $\theta = 0$ deg and infinite apparent wavelength) stacking with and without time shift is equivalent. In reality (i.e., for most array and source geometries), applying time shifts will increase the chance for coherent summation by improving waveform alignment, therefore, the only advantage of detection-only methods is the drastically reduced computational cost by avoiding the spatial grid search.

Practical implementation of detection-only methods ensures coherent waveform summation by restricting inter-station distances. The initial array is typically divided into small subarrays (or patches) and only waveforms within the same patch are stacked without time shifts. The resulting patch stacks are then combined in some way. For example, Meng and Ben-Zion [30] divide an 1108 geophone array (600×600 m^2) along the San Jacinto fault zone into nine patches of 200×200 m^2 within which they stack station waveforms without time shift.

They multiply the envelopes of each patch stack to produce a single time series on which they perform amplitude triggering and attribute high values to detection of weak earthquakes. For each detection they go back and beamform (i.e., stack with time-shift) using the nine patch envelopes to estimate a source location.

The detection method of Li et al. [90] is nearly identical, except that within each patch (each station and its four nearest neighbors) they stack inter-station cross-correlations instead of the raw waveforms. They then sum the envelopes of each patch stack and perform amplitude triggering for detection. They apply this technique to the Long Beach nodal array to detect aftershocks associated with the Tohoku-Oki earthquake. The main issue with restricting inter-station distances (necessary for stacking without time shift) is to limit the number of possible stations that can be summed coherently. This has important implications for detection thresholds, which will be demonstrated in the following sections. A different type of detection-only method, that of Seydoux et al. [32], uses the width of the cross-spectral density matrix eigenvalue distribution to analyze the spatial coherence of the seismic wavefield. Since the number of non-zero eigenvalues is related to the number of independent signals [95], an earthquake that is coherent across the entire array is associated with a single dominant eigenvalue while many surface wave sources result in a flatter distribution of eigenvalues. They use this method to detect teleseismic earthquakes and seismo-volcanic events at Piton de la Fournaise. One potential weakness of this method is that a single strong contaminating surface source will also appear as a dominant eigenvalue.

One important variable in beamforming methods is the processing of the

original waveforms prior to stacking. For example, Hansen and Schmandt [31] beamform using the STA/LTA of individual station recordings on the Mount St. Helen's seismic array to search for events associated with volcanic activity. The weaknesses of migrating purely amplitude data (e.g., STA/LTA envelope, etc.) is the requirement that event arrival waveforms have SNR > 1 on the raw seismograms, whereby valuable information on waveform coherency is discarded. In another study, Inbal et al. [91] beamform using the envelopes of signals created by stacking without time shift of each station with its four nearest neighbours (i.e, requires SNR > 1 after 4 stacks). They use this method to detect and locate seismicity occurring beneath the Long Beach, California surface array. Other pre-processing options include the sliding-window kurtosis [94] or cross-correlations [20] of the original waveforms.

These beamforming-like techniques are part of an even more general framework called matched-field processing [56], which involves the comparison of data recorded at a station array with synthetic data generated by a wave propagation model. Examples of this method applied in seismology include locating bubble collapse events to map hydrothermal systems [58] and locating microseismic events associated with hydrocarbon extraction [59]. In this framework, beamforming can be thought of as the special case where the synthetic signals are appropriately shifted delta functions.

In summary, there are many different methods to detect and locate seismic sources using continuous data recorded on dense arrays. The majority of these methods involve the stacking of signals recorded at different stations either with time shift (beamforming), without time shift, or some combination thereof. The methods also vary in the processing of the signals prior to stacking. In this paper,

we develop a general processing framework for the detection and location of seismic sources using continuous data from large-N arrays. We begin with a description and justification for each processing step, followed by a synthetic example to demonstrate different aspects of the processing. Next, we look at a real dataset resulting from a 10,050 node passive survey that was deployed to evaluate the suitability of a 3×3 km^2 piece of land for carbon sequestration. Using our workflow we detect and locate different sources of seismic energy and discuss the minimization of artifacts generated by coherent contaminating sources.

4.3 Methods

Here we propose a general processing framework for the detection and localization of seismic sources using data recorded on one-component geophone surface arrays. With only vertical component surface stations, we attempt to maximize the contribution of P-wave energy originating below the array while suppressing contaminating surface sources. We also seek a method that exploits waveform coherency to allow for the detection of events with signal-to-noise ratios measured on single seismograms much less than one. The final constraint is that the resulting method must have reasonable computational costs, where we define reasonable as the ability to process typical large-N array datasets (1-50 TB) on a single processing server (e.g., 20 cores, 200 GB RAM) in 1-5$\times$ real-time. Based on these constraints, our processing is as follows:

1. Decimate data
2. Stack nearby inline stations without time shift

3. Window and pre-process waveforms
4. Beamform with sub-arrays (patches)
5. Infer detections and locations

To help illustrate aspects of the processing, we use a synthetic acoustic example [67] consisting of a single source (80 Hz Ricker wavelet with M_w=-0.5), a homogeneous velocity model (3000 m/s), mid-quality sedimentary rock Q=150 and 10,050 stations (Fig. 4.1) with 10 m and 100 m inline and inter-line spacing, respectively. The choice of these source and station properties is meant to emulate the real dataset studied in Section 4.4.

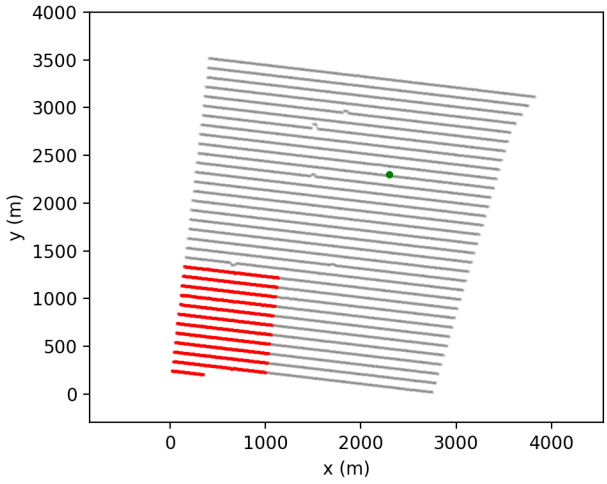

FIGURE 4.1: Setup for the simulation with 10,050 surface stations (gray dots) and the source (green dot) located at [2300, 2300] and 1200 m below the surface. Stations are grouped into nine equally sized patches (example of one such patch in red). Stations appear as single line due to the close (10 m) inline spacing.

4.3.1 Frequency selection and data decimation

The purpose of downsampling is to reduce the size of the dataset for computational efficiency. With the decimation factor dictating the highest resolvable

frequency, selecting an appropriate decimation factor depends on the expected frequency content of the arrival waveforms. This frequency content depends primarily on the source properties (e.g. magnitude, stress-drop, mechanism etc.), distance from source to stations and the rock quality factor Q (typically Q=25-500 for sedimentary rocks). A comparison of different rock quality factors for a M_w-0.5 event can be seen in Fig. 4.2. The value of Q dictates the amount of intrinsic attenuation incurred by propagating waves and thus largely controls the peak frequency of the recorded arrival waveforms. For our case of lower grade sedimentary ($Q = 150$) we expect microseismic events will have stress drops on the order of 0.1 MPa and thus peak frequencies of 30, 100 and 800 Hz for M_w= 0,-1 and -2 respectively [96] (see Fig. 4.3).

Based on these assumptions, an upper corner frequency of at least 100 Hz would preserve the majority of energy for microseismic events down to M_w-1. In practice however, we are also limited by our uncertainty in the estimated velocity model. Since our method seeks to exploit coherent summation of arrival waveforms, even small traveltime errors at higher frequencies can cause destructive interference. Although this is a non-issue with synthetic data where we can compute traveltimes exactly, to be consistent with velocity uncertainties in the real dataset we set our upper corner frequency to 50 Hz.

4.3.2 Stacking without time shift

This step involves summing the raw waveforms of spatially close stations into a single averaged waveform with the primary purpose of data reduction. The location of the 'stacked' station is set as the centroid of the binned station locations.

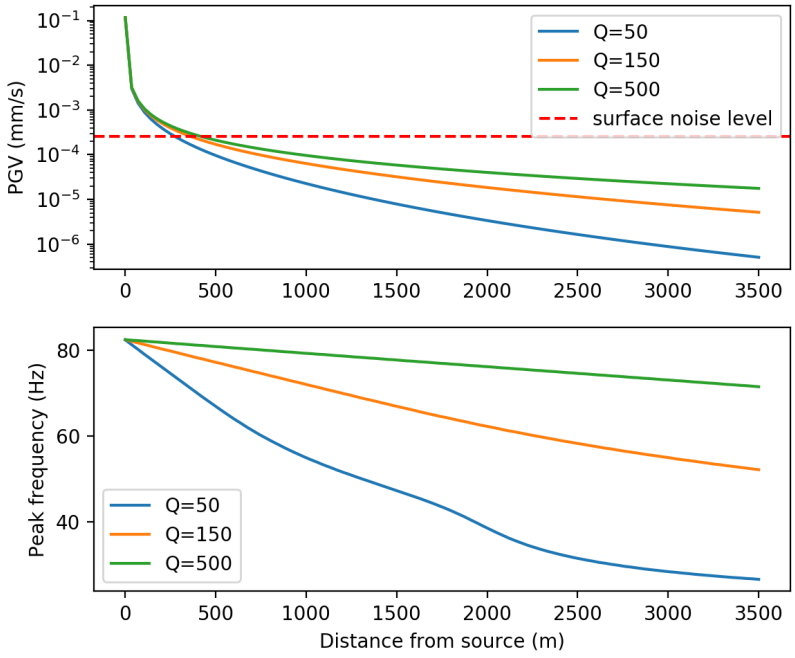

FIGURE 4.2: The effect of attenuation on arrival waveforms for three different rock quality factors (source is a M_w-0.5 Ricker wavelet with 80 Hz center frequency). Top: Peak ground velocity (PGV) of arrival waveforms as a function of distance from source with red dashed line showing noise level typical of surface arrays (i.e. all arrival waveforms beneath noise level for distances over 500m). Bottom: Peak frequency of arrival waveforms as a function of distance from source.

To prevent destructive interference of event arrival waveforms, stacking without time shift should only be used for groups of stations where the maximum inter-station distance is several times less then the shortest expected apparent wavelength. To determine whether stacking nearby stations without time shift is appropriate in the synthetic example, we assume that microseismic events are occurring in the middle of the array at 600 m depth (xyz=1700,1700,600) and are traveling in a constant $c = 3000$ m/s velocity medium. With an upper corner frequency of $f = 50$ Hz , the apparent wavelength at the edge of the array is $\lambda_a = c/(f \sin\theta) = 70$ m, which indicates destructive interference can occur for

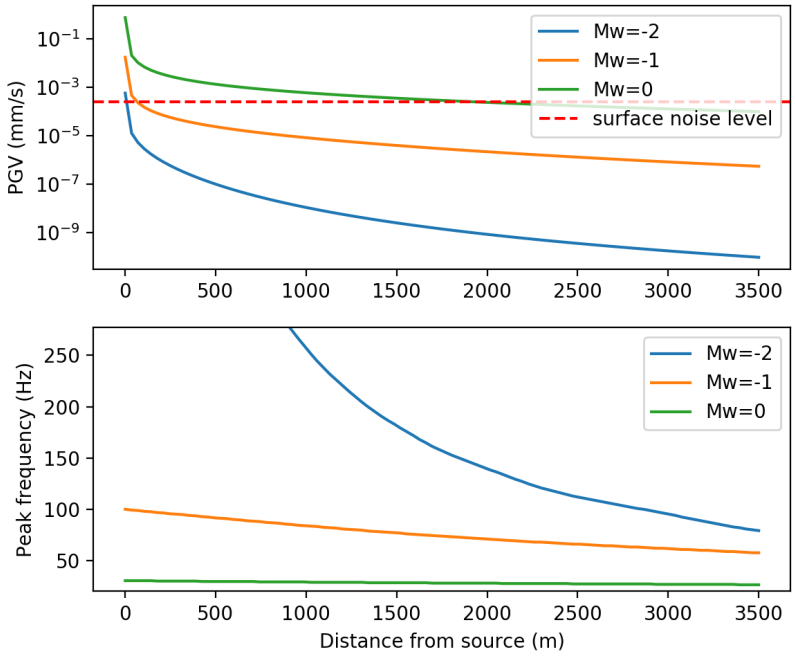

FIGURE 4.3: Plots comparing peak ground velocity and frequency content for synthetic sources with three different magnitudes for Q=150. Top: Peak ground velocity as a function of distance with red dashed line showing noise level typical of surface arrays. Bottom: Peak frequency as a function of distance (note M_w=-2 has a peak frequency of 800 Hz at source location.

any inter-station distance over 35 m. Based on this value, we would only stack waveforms for stations separated by less 35 m, which limits us to combining each three adjacent inline stations.

Although stacking without time shift is appropriate here (and leads to similar results), we choose not to apply it for this synthetic demonstration. While this step has the added benefit of constructively interfering arrivals with high apparent velocities (typically P waves generated at depth) while destructively interfering slower propagating arrivals from surface contaminants (Rayleigh and sound waves), a similar effect is realized when migrating the original waveforms into 3D space at P-wave velocities. Thus the primary purpose of this step remains

data reduction.

4.3.3 Waveform windowing and pre-processing

Selecting appropriate time windows to shift and stack waveforms is an important step and the best method will depend on the specific application. Here we will discuss two different approaches and then present our solution, which combines aspects of both.

The first method involves treating each sample index as a potential origin time, for which a grid search is performed. At each location in the grid search, a custom time window would be computed for each station (based on source-station travel time and source duration) and the signals within these windows for each station would be processed and stacked. While custom time windows are the most appropriate way to apply time shifts, new data selections for each source origin time and grid location result in a high computational cost when further processing (e.g., whitening, cross-correlation etc.) must be performed within each selected window. This method is still suitable for small datasets, or when the data processing can be performed only once to the entire dataset (e.g., STA/LTA) prior to grid-searching.

A more common approach is to split the data into fixed overlapping time-windowed segments (i.e., each segment contains the same time period for all stations) and perform one grid search per segment through repeatedly time shifting and summing the same pre-selected waveforms. The main advantage of this method is that any processing of the waveforms (including cross-correlations) need only be applied once prior to the search. The primary limitation of this method is that by using the same time window for all stations, the minimum

window length must be increased to account for the greatest travel-time difference expected for any source location. The difference between this window length and the source duration dictates the amount of unnecessary signal that is potentially being summed. In our case, given a wave velocity of 3 km/s and maximum inter-station distance of 3 km, we would require at minimum a one second time-window for a source originating at any location to be recorded at all stations. For microseismic sources with a typical source duration of $\sim$100 ms [96] that generate signal-to-noise ratios (SNR) equal to one over the array, over 90% of the total energy included in the fixed window is noise. While uncorrelated random noise will destructively interfere during stacking (see Section 4.3.4), coherent noise generated by contaminating sources is not as easily removed (see Section 4.4.2).

We therefore seek a method that utilizes custom time windows but also allows for windowed pre-processing of the waveforms prior to searching. Our solution is similar to the first method above, in that new data selections are made at each station for each grid location; however, instead of building custom time windows centered around the predicted arrival at each station, data selection involves a choice amongst pre-built overlapping windows. Selecting from existing time windows requires applying a small time shift to each waveform equal to the difference between the theoretical and actual window start time to ensure proper waveform alignment. The advantages of this method are: (1) selecting time windows for each grid location removes minimum window length requirements and improves the SNR; and (2) making this selection amongst precomputed windows allows for most waveform processing to be done once, prior to beamforming.

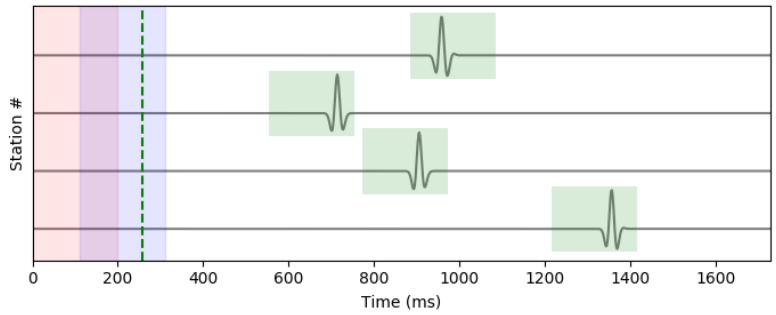

FIGURE 4.4: Synthetic data for five random stations. Preprocessing involves splitting the data into overlapping windows (overlapping red and blue shaded areas show the first two out of 14 windows in this example). A grid search is then performed for each potential origin time (green dashed line shows true origin time) where pre-determined time windows are selected based on source-station travel times for each station. The green rectangles show window selections for the true source location and origin time. Waveforms in these windows are then rolled using the exact time shift and stacked.

For the synthetic example, we split the data (Fig. 4.4) into 50% overlapping, 200 ms time windows. Although the optimal window length in this case would be equal to the source duration (50 ms), a longer window is used for illustration purposes. For a given origin time and source location, time windows are selected for each station, shifted and stacked. Although waveforms are shown in the time domain, in practice we stack their complex phases (i.e., whitened spectra). The beampower at a given grid location is then calculated as the energy of the final stack normalized by the number of stacks.

4.3.4 Dividing array into sub-arrays

Instead of performing a grid search with all stations simultaneously, we divide the array into patches and allow each patch to perform its own grid search

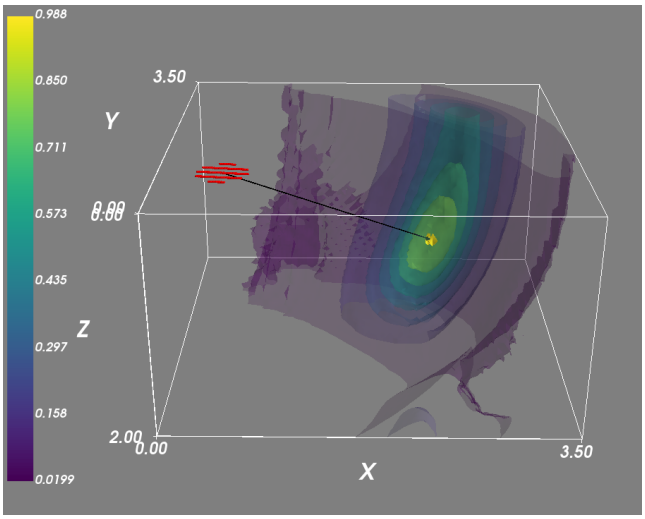

FIGURE 4.5: Beamforming results for synthetic data using 140 stations (red) with colored contours describing stack coherence, where one is perfect score. Maximum coherence is obtained at the true source location. Note the spherical shape of the location uncertainty due to this source-station geometry. The search grid is $3.5 \times 3.5 \times 2$ km^3 at 50 m spacing.

(Fig. 4.5). Constraining inter-station distances increases robustness to uncertainty in the estimated velocity model and heterogeneities that are unaccounted for (e.g., scatterers, reflectors). By sharing similar ray paths to any potential source location, arrivals should have high waveform similarity (e.g., polarity, coda) and more systematic errors in estimated travel times. These properties greatly increase the chance for coherent waveform summation. The disadvantages of using patches are that: (1) the detection threshold is limited by number of stations in a given patch; and (2) the effective array aperture is reduced to the patch dimension, increasing location uncertainty. However, if we assume that a potential microseismic event will be weak and the coherency of its arrival waveforms will degrade as inter-station distance increases, then this trade-off is acceptable. In our synthetic example (perfectly estimated medium) there is no advantage to using patches.

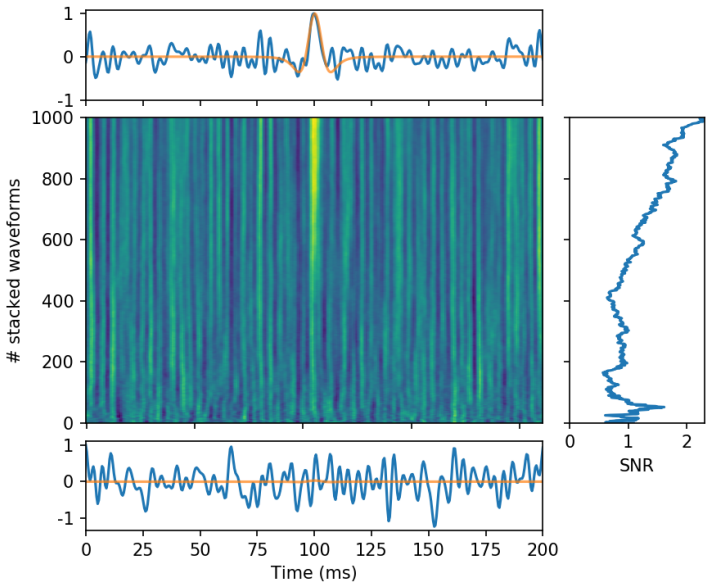

FIGURE 4.6: The importance of stacking to detect coherent arrivals buried in uncorrelated noise. Bottom: Original synthetic waveform (orange) and same waveform with additive noise (blue). Noisy signal has a PGV ∼45 times greater than the original signal. Middle: Cumulative summation of these noisy waveforms for stations in one patch (from Fig. 4.1) and SNR for each successive stack (right panel). Top: Final stacked waveform (blue) compared again with the original waveform (orange).

The best patch size is found by determining the minimum size that will sum the highest number of waveforms coherently. This needs to be determined experimentally, but our recommendation is to start with several large patches and shrink if needed. To demonstrate the importance of stacking a high number of waveforms, uncorrelated random noise is added to the original synthetic waveforms (comparison in bottom panel of Figure 4.6). The PGV of the noise ($2.5e^{-4}$ mm/s) added to each station is between 5-50$\times$ higher (depending on distance) than the PGV of the raw arrival waveforms. The waveforms are then

aligned and cumulatively summed (middle panel Figure 4.6) and the SNR is calculated for each stack number. Note how the arrival only becomes clearly visible after stacking about 800 stations.

4.3.5 Inferring detections and locations

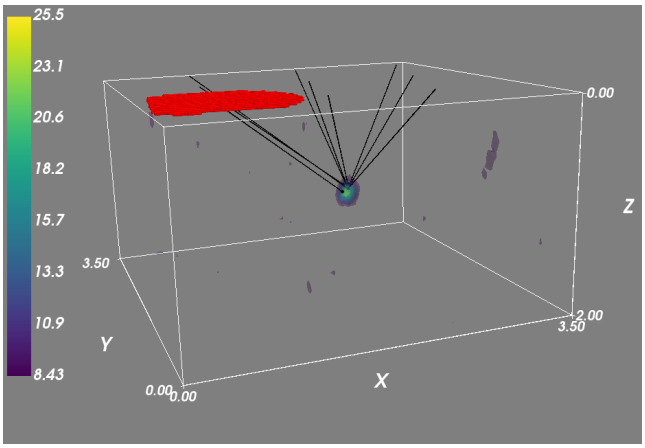

FIGURE 4.7: Beamforming results for all patches using the noisy synthetic data. Colored contour values represent the median absolute deviation output power for the patch whose stations are highlighted in red. Each patch has a black vector from its center to its respective grid maximum. Although some patches have slightly mislocated the source, their combined maximum is at the true location.

For each potential origin time, a beamforming output grid is produced for each patch. In each of these grids, the maximum value and its grid location are recorded. Grid values are converted to deviations from the median via the median absolute deviation MAD$= med(|x[i] - med(x)|)$ metric. This is preferable to the standard deviation metric as the median is more robust to outliers than the mean in the presence of a source.

Results using this noisy synthetic data can be seen in Figure 4.7 with a vector drawn from the center of each patch to the location of its respective grid maximum. In addition, the absolute grid values from all patches are summed into a combined grid from which a most likely source location and output power (median deviation) for the entire array is obtained. If the patch sizes are reduced to 500 stations each, this event is no longer detectable.

We infer positive detections by looking for relatively high output values (compared to other time windows) as well as obvious clustering of the most probable source locations for each patch. These choice are highly subjective and will depend mainly on array geometry, grid size and presence of contaminating sources (see Section 4.4.3).

4.4 Application to carbon capture and sequestration

Climate change due to the excessive release of anthropogenic carbon dioxide (CO_2) emissions into the atmosphere is perhaps today's most important environmental issue [8, 9]. One potential solution to curb emissions is carbon capture and sequestration (or storage), abbreviated CCS [10, 11, 12]. This process involves capturing CO_2 from large point source emitters (e.g., coal or gas fueled power plants), transporting (typically via pipeline) it to a storage site and injecting it deep underground. Geological storage of CO_2 requires injection at depths of over 1000 m below the surface where temperature (>31°C) and pressure (>100 atmospheres) conditions are suitable for supercritical carbon dioxide [10]. Injection typically occurs into a target saline formation overlain by a highly impermeable caprock layer that prevents escape of CO_2 to the surface. There are

currently 37 large scale CCS projects worldwide, with 17 in operation and the remainder in varying stages of development [12, 97].

Despite the success of these projects, there are still concerns surrounding this new technology, primarily from induced seismicity and the potential for CO_2 leakage [98]. With a major leak from the storage reservoir negating all positive benefits of CCS, the detection, mitigation and remediation of leakage has recently emerged as an area of research interest [12]. Passive seismic monitoring of micro-earthquakes has proven a crucial tool to understanding both the migration patterns of the CO_2 plume and the geomechanical response of sites to injection [24, 25, 26]. Risk can also be reduced pre-injection through proper site selection and understanding the existing geology. The purpose of our work is to delineate any pre-existing fracture networks or zones of weakness by studying the passive microseismicity in the area before injection. This information could then be compared with predicted CO_2 plume migration to improve risk modelling.

4.4.1 Dataset

This dataset is the result of a five-day surface array deployment consisting of 10,050 nodal 10 Hz geophones arranged with 100 m inter-line and 10 m in-line spacing to cover an approximately 3×3 km^2 area in Queensland, Australia (Fig. 4.8). The array was primarily deployed to record an active source vibroseis survey that used P-waves reflections to determine the depths to various geologic layers (in particular the seal layer at around 1200 m depth). The active survey took five days, during which data were continuously recorded at a sampling rate of 1000 Hz, resulting in a dataset of approximately 20 TB. Our work

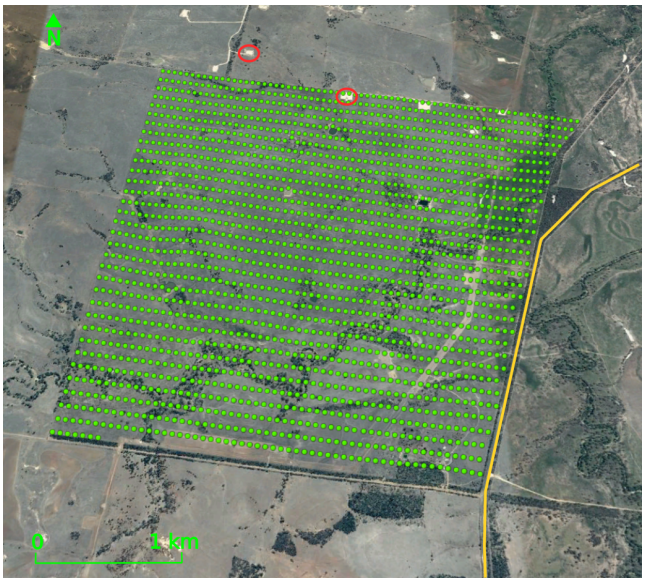

FIGURE 4.8: Map of the 10,050 geophone surface array deployed over a five-day period in Queensland, Australia. Every fifth inline station is plotted as a green dot for clarity. There is a local highway (yellow line) adjacent to the array as well as several coal cleat gas pumping stations in the area (white rectangles). The two pumping stations that are most active during the survey are circled in red.

focuses on processing the passive dataset (i.e., time periods excluding shots) to characterize any naturally occurring seismicity in the area. Based on the location and rate of detected microseismicity, we hope to identify any potential fracture networks and evaluate the risk they pose to carbon sequestration.

4.4.2 Contaminant sources

Prior to searching for microseismic events, we attempt to locate any persistent contaminating sources within or near the array. Our first approach is to plot peak ground velocity at each station within ten-second time windows and look for spatial patterns (Fig. 4.9). Examples of the waveforms recorded at stations nearby each identified source can be seen in Figure 4.10.

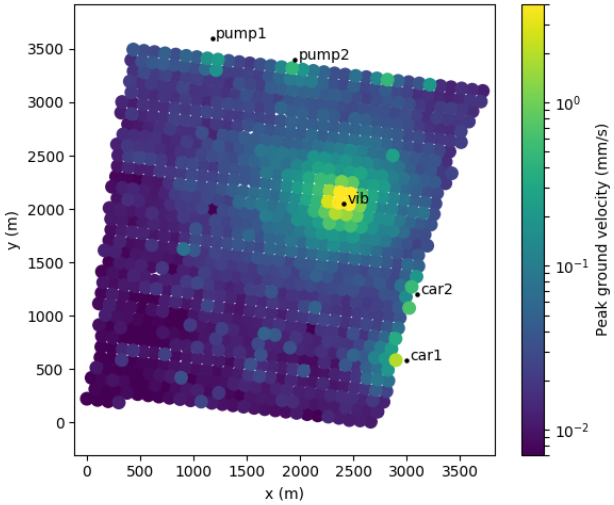

FIGURE 4.9: Peak ground velocity at 1000 stations for a ten-second time window with anomalies labeled by their respective source (pumping stations, vibroseis sweep and cars traveling on highway). The color scale is logarithmic and amplitudes have been saturated at 4 mm/s (from 15 mm/s at closest station to vib).

The strongest source is a vibroseis sweep that lasts about seven seconds and generates strong P waves over a wide frequency band (i.e., a chirp signal). An example of beamforming during a sweep can be seen in Figure 4.11. In theory, each strong subsurface reflector should act as its own source and thus be detectable through beamforming (typically referred to as diffraction imaging). While it is possible that the observed feature at 1200 m depth in Figure 4.11 is caused by a strongly reflecting layer, synthetic tests would be needed before any definite interpretation can be made. Although not shown here, these sweeps were helpful in improving our velocity model through iteratively determining the velocities that maximize the summed output power.

Considerably weaker sources of seismic energy are vehicles traveling on nearby roads. An example of tracking a single vehicle is shown in Figure 4.12 where longer time windows (four seconds) and lower frequencies (8-20 Hz) are used

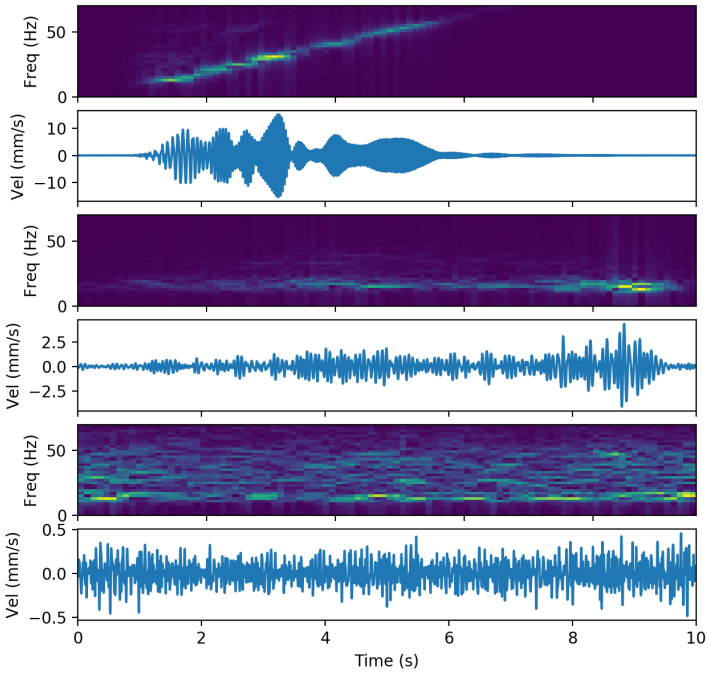

FIGURE 4.10: Spectrogram and waveforms for vibroseis sweep (top), moving vehicle (middle) and pumping station (bottom). Waveforms are taken from the closest station to each respective contaminant source during the same time window as Figure 4.9.

in the processing to enhance these P-wave arrivals. In this case, even the furthest patches (6 km from road) are able to detect and roughly locate the vehicle, despite large uncertainties and scatter. Repeated beamforming over time is able to track the vehicle traveling roughly WNW along the highway at a speed of approximately 70 km/h. The ability to track single cars traveling on a distant highway implies that the method is robust to sources that occur outside of the grid, and that microseismic sources that produce similar ground velocity perturbations should be detectable.

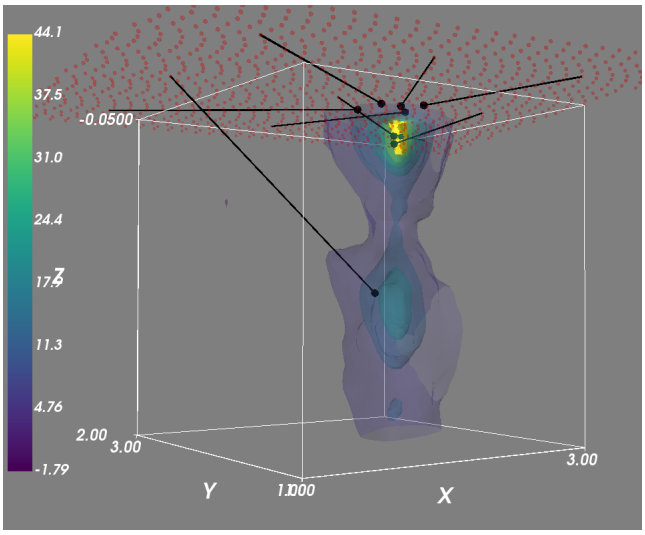

FIGURE 4.11: Colored contours showing combined output power during a vibroseis sweep. Vectors are plotted from each patch center to their respective maximum grid location. The local maximum at 1200 m depth could be caused by a strongly reflecting layer that appears as its own source.

Individual seismic arrivals from these sources are not visible on single seismograms; however, visualizing the stacking process is helpful to get an idea of their strength. Using stations from the lower middle patch in Figure 4.12, we compare stacking with several different beamformer configurations in Figure 4.13. It takes stacking of at least 200 waveforms before the vehicle (blue) is detectable when compared to the null case of stacking random noise (red). However, since surface array noise is typically correlated, a more accurate null case is to use the same real data but point the beamformer (i.e., align the waveforms) to a location where no source is present. When compared to this new null case (orange) the vehicle is only detectable after stacking at least 500 waveforms.

To compare with a source that has visible arrivals at most stations, we point the beamformer towards a pump location (see Figure 4.8) and align the waveforms using the acoustic velocity of 345 m/s. In this case (green) the coherent

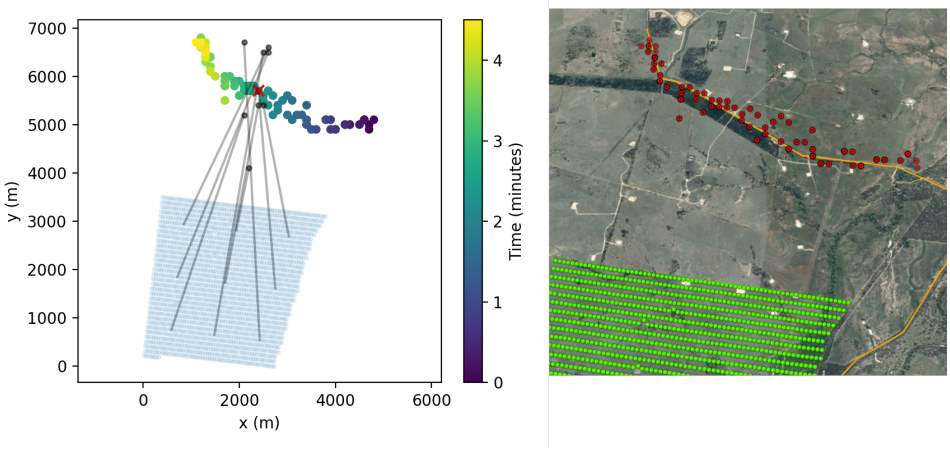

FIGURE 4.12: Example of tracking a moving vehicle on a nearby road with a four-second window length and origin time step of two seconds. Left: Black vectors show individual patch locations for a single origin time (combined location as red cross) whereas colored circles show the location of the combined grid maximum for every time step. Based on the vehicle's location over time, we estimate an average speed of ∼70 km/h. Right: Same locations (red circles) plotted over the map for context with road highlighted in orange.

summation is immediate and the energy of the final stack is about an order of magnitude higher than that of the vehicle.

The broadband acoustic waves generated by the coal cleat gas pumping stations are coherent across the entire array and create artifacts even when beamforming at P-wave velocities. To understand the potential artifacts they create, we use a synthetic example with a persistent source at the location of the left pump emitting waves traveling at the speed of sound in the air. Beamforming is then performed with this synthetic data but using P-wave velocities ($\sim$ 3000m/s) to compute travel times and the output power is plotted for a single patch (Fig. 4.14). Although there is no clear focal point indicative of an accurately located source, a significant amount of coherent summation occurs at certain grid locations which could lead to many false detections when searching for microseismic events at P-wave velocities.

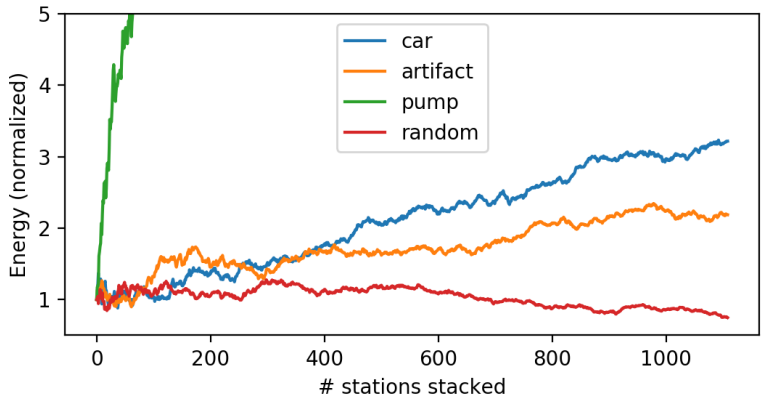

FIGURE 4.13: Figure comparing stack energy as a function of number of stations stacked for the lower middle patch in Figure 4.12 with each plotted line corresponding to a different beamformer configuration. Blue: waveforms aligned to location of vehicle using P-wave velocities. Orange: waveforms aligned to center of patch using P-wave velocities. Green: waveforms aligned to pump location (left pump Figure 4.8) using acoustic velocity (clipped but reaches a maximum energy of 25). Red: null case with original waveforms at each station replaced with random uncorrelated band noise.

Artifacts depend on the source-station geometry and they are unique for each patch. In this case the lower left patch (shown in Figure 4.14) consistently generates the most false detections due to its unfavorable station orientations with respect to the acoustic source. Although the acoustic waves generated by the pumping station travel relatively slowly, they arrive nearly simultaneously at multiple inline stations for this patch. Coherent summation is therefore realized at locations where the travel-time differences to groups of these inline stations is minimized.

Although the pumping stations have known locations and acoustic wave velocities, we have not yet found an effective way to remove their contribution to the waveforms recorded at each station. The most promising methods, those

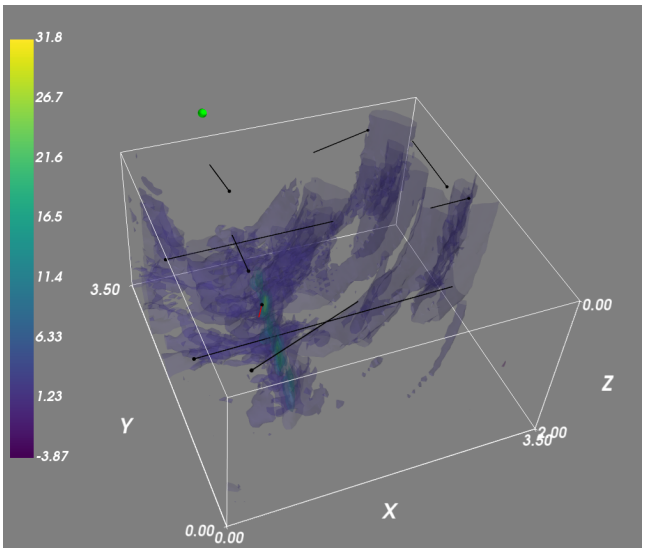

FIGURE 4.14: Synthetic example to show artifacts (volumes of coherent summation) caused by acoustic waves generated by pumping station for the bottom left patch (red vector) when beamforming at P-wave velocities. Maximum artifact locations for all other patches drawn as black vectors.

that rely on reconstructing the cross-spectral density matrix array (CSDM) using only a subset of eigenvalues (where typically the first few are excluded as these correspond to the strongest coherent sources) require long time windows to allow for the direct acoustic arrival to reach all stations and are therefore not suitable for our purposes.

To reduce the contamination from the pumps when searching for potential microseismic events, short 100 ms time windows are used to relatively enhance the energy of any potential impulsive arrivals. Additionally, the strongest artifact locations are estimated for each patch and the beamformer is prohibited from searching in these locations (Fig. 4.15). Estimating the artifacts for a single patch involves beamforming and averaging the output grids for hundreds of potential origin times. Based on this average grid, locations where values exceed a certain threshold are excluded from future searches.

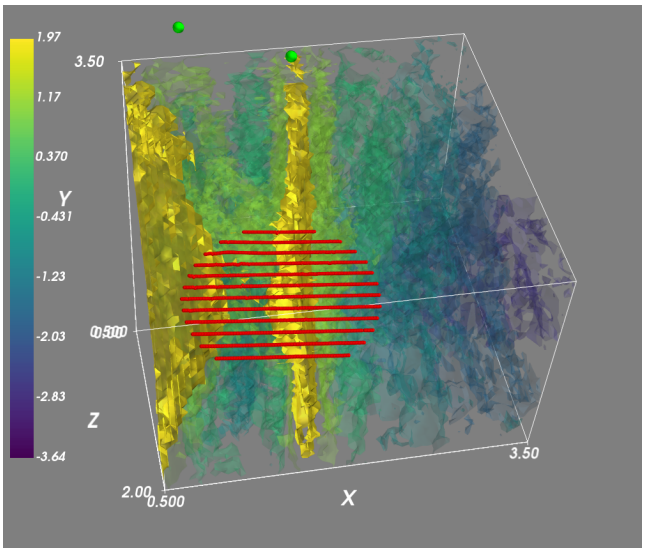

FIGURE 4.15: Real artifacts caused by acoustic waves from pumping stations (green spheres) for the bottom middle patch (stations in red) when beamforming at P-wave velocities. Maximum values are clipped at a given threshold (two deviations from median in this case) and the beamformer is prohibited from searching these locations in subsequent searches. In this case, nine percent of grid locations are prohibited.

4.4.3 Potential microseismic events

Before searching for real microseismic events, we develop a rough estimate of potential detection thresholds based off our source-station geometry, rock quality Q (estimated at 150), upper corner frequency (at which coherent summation is expected) and the surface noise level. Since we are interested in events around 1000m depth (caprock) and near the array center, the mean of source to station distances (1800 m) is used to calculate attenuation. The upper corner frequency is dictated by the highest frequency at which coherent summation is expected. In this case, uncertainties in our velocity model (1D layered) limit us to 50 Hz which was determined by shifting (based on our velocity model) and stacking vibroseis arrival waveforms at distant patches. Since the sweeps

span all frequencies we determined the frequency at which the signals begin to destructively interfere due to improper shifts. Lastly, since the vibroseis trucks are nearly continuously active during the daytime, we focus on processing the nighttime data for potential microseismic events. During quiet time periods (and away from acoustic contaminants) peak ground velocity is on the order of 10^{-4} mm/s (same noise level used in synthetics).

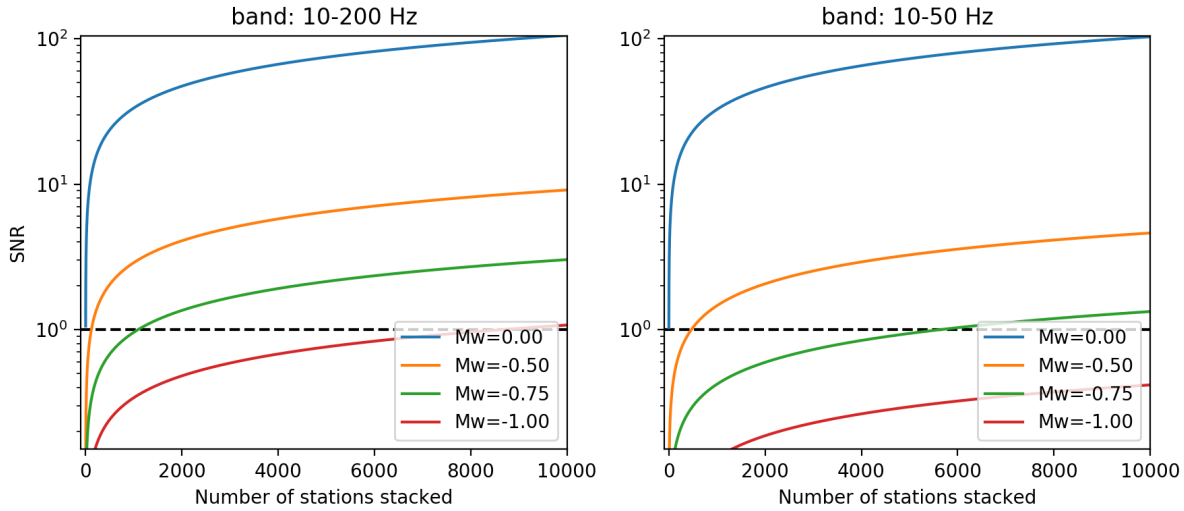

FIGURE 4.16: Plots comparing SNR as a function of number of stacked synthetic arrival waveforms for different moment magnitudes and frequency bands 10-200 Hz (left) and 10-50 Hz (right). The synthetic waveforms were computed with parameters: Q=150, 1800 m distance to source, and noise level= 2.5×10^{-4} mm/s. Points with SNRs greater than one (dashed line) we consider detectable. For example the arrivals from the M_w0 event would be visible on a single station trace (for both bands) while the M_w-0.5 event would only be detectable after stacking 140 or 460 arrival waveforms in the left and right case respectively.

Using these parameters in a synthetic example helps us estimate the detectability of different magnitudes as a function of number of stacked stations (Fig. 4.16 right panel). Although these results are based off uncorrelated noise, we are confident that real events with magnitude equal to or larger than M_w-0.5

will be detectable after stacking waveforms within each patch (1000 stations) coherently and combining patches results incoherently. It is important to note that our upper corner frequency of 50 Hz greatly limits our ability to detect events below M_w-0.5. Increasing the upper corner frequency (Fig. 4.16 left panel) greatly improves detectability of weaker events but requires a better estimated velocity model.

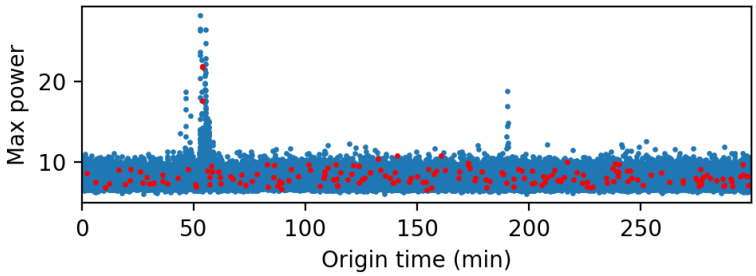

FIGURE 4.17: Maximum combined output power of beamformer (units in MAD) for five hours of nighttime data. The strong peaks around 50 and 190 minutes are caused by vehicles passing nearby. Times colored in red indicate periods where strong clustering of patch locations were detected (3 or more locations within 250 m of each other).

Using this processing, the results of searching five hours of nighttime data for microseismic events can be seen in Figure 4.17. Even though our search grid excludes the nearby roads, the strong peaks in combined output power are caused by vehicles passing nearby. Ideally, a microseismic event would have both relatively high output power and strongly clustered patch locations. So far we have not seen any time periods where this is the case, as origin times with high clustering appear to be quite random and mostly uncorrelated with output power. Although we have only looked at about one tenth of the total nighttime data, these findings suggest no microseismic activity above M_w-0.5 is occurring beneath the array.

Going forward, alternative methods for removing contaminant sources are required. The most obvious solution is to shut down pump activity during the seismic recording period. Another possibility involves burying the geophones deeper in the ground to reduce air-ground coupling effects; however, this solution is likely not cost-effective. Alternatively, it might be possible to remove the source-time function of the pump stations through deconvolution. To achieve this, extra sensors can be installed at each pump location, whose recordings can be deconvolved from seismograms recorded at every sensor within the array. Problems can still arise when multiple pumps are active simultaneously, thus producing interference patterns that strongly bias the deconvolution process.

Finally, the detection of moment magnitudes less than -0.5 will likely only be possible with a higher upper corner frequency. This would require minimizing errors in traveltime differences, either through better estimation of the velocity model or using smaller patch sizes (i.e ensuring similar raypaths). The trade-off with smaller patch sizes is less potential for coherent summation.

4.5 Conclusion

In this paper we developed a dense surface array processing framework for the detection and location of microseismic events. Our processing involves: (1) reducing the data volume through decimation and stacking of waveforms at adjacent stations; (2) dividing the array into smaller sub-arrays, or patches; (3) processing the waveforms (spectral whitening) within fixed overlapping time windows; (4) selecting the appropriate time windows based on a grid search for source locations; (5) stacking the time-shifted seismograms using the exact source-station travel times within each patch; and (6) combining the output from

all patches to infer detections and locations of sources. This processing framework is demonstrated using a synthetic example and is shown to be robust even in the case where the signal-to-noise ratio on single waveforms is well below one.

Next we applied this processing to a real dataset from a carbon sequestration project to monitor microseismic activity. Using these data, we identified contaminant sources that dominate the waveforms, such as vehicles traveling along highways surrounding the array and sound waves produced by nearby pumping stations. The signals created by these sources can potentially bias the recovery of true microseismic events, and we propose a method to minimize these artifacts through synthetic modeling. Based on properties of the dataset we estimate our processing is able to detect events of moment magnitude -0.5 and above. While we cannot dismiss the possibility of small microseismic events below M_w-0.5, we detect no events larger than this suggesting this is likely a good repository for carbon storage.

Additional work is needed to further assess the possible presence of smaller event activity and pre-existing fracture networks. This includes new methods for the removal of contaminating noise sources that limit the detection threshold. Possible solutions include burying the sensors to reduce contamination by acoustic waves propagating in the air, or placing microphones at each pumping station to record and deconvolve the associated source-time functions.

Chapter 5

Conclusion

5.1 Summary of chapters

Our increasing interaction with the Earth requires techniques for monitoring its response and seismology provides many tools to accomplish this. Although seismic systems are already widely used in industry, many of the current processing techniques are outdated. For example, the routine detection and location of seismic sources is still predominantly accomplished using triggering and phase-picking methods, which fail for sources that are persistent, weak or simultaneously active.

The detection and location method (InterLoc) we present in Chapter 2 is an effective and automated solution to this problem. The success of this technique lies in the robustness of cross-correlations, the insensitivity to environmental conditions exhibited by spectral whitening, and the localization advantages of a steered beamformer. We demonstrate the effectiveness of this technique by monitoring both impulsive and persistent sources at two active underground mines. Additionally we propose how this information on source locations and

activity can be integrated with ambient noise interferometry to improve recovery of estimated seismic Green's functions.

While traditional seismology focuses on natural sources (e.g. earthquake rupture), industrial environments are also host to many anthropogenic sources of seismic energy. Typically seen as contaminants, we show in Chapter 3 how (once located) these 'unconventional' seismic sources can be exploited to perform sensitive monitoring of the rockmass. Our specific application use seismic energy generated by ore crushers to track the growth of a block cave at an active underground mine. This technique involves cross-correlation of signals recorded at a sensor pair where at least one source-sensor ray path crosses an area of interest. From the resulting cross-correlation functions, we measure travel-time changes and attribute them to the additional path length incurred by the crusher-sensor ray paths having to circumvent the growing cave. In addition to other anthropogenic sources (e.g. vehicle traffic, cities, industrial machinery), this technique could also be used with persistent natural sources such as volcanic tremor, hydrothermal bubble cavitation and microseisms.

In Chapter 4 we return to source localization, but this time we develop a processing framework for dense, or large-N, surface arrays. These deployments are becoming increasingly popular for the detection and location of weak microseismic events as the coherency of arrival waveforms recorded across the array can be exploited through waveform stacking. Our proposed method takes full advantage of this while maintaining reasonable computational costs. The processing involves: (1) reducing the data volume through decimation and stacking waveforms at adjacent stations; (2) dividing the array into smaller sub-arrays to ensure waveform similarity; (3) pre-processing of the waveforms within short

fixed time windows; (4) selecting the appropriate time windows based on a grid search for source locations; (5) stacking the time-corrected windows based for each sub-array; and (6) combining the output from all sub-arrays to infer detections and locations of sources. The processing is validated by locating a variety of sources from both synthetic data and a real dataset from a carbon sequestration project. We also discuss the effect of coherent contaminating sources (typically anthropogenic sources at surface) and how these artifacts can be minimized.

The techniques we develop have direct industrial applications in mining, carbon sequestration, exploration, geothermal and hydrocarbon extraction operations. However their application also extends to natural setting such as earthquake seismology, volcanic monitoring, fault detections and hydrothermal system monitoring.

5.2 Future work

Due to the high costs of drilling, it is likely that the majority of continuous seismic data will continue to originate from surface arrays. Relative to the fixed costs associated with a deployment of a surface array, the marginal cost of additional stations continues to decrease. For these reasons we believe methods for processing continuous datasets generated by large surface arrays will become increasingly important.

In addition to instrumentation, seismic methods depend on sources of seismic energy. In most cases, controlled active sources would produce the highest quality data, however (barring some large technological advance) these sources

will remain expensive and impractical to operate on long time scales. The greatest potential for improvement lies in utilizing the already available sources of seismic energy through the processing of passive continuous datasets. This is challenging when either no suitable sources are available, or where there exist strong contaminating sources.

When no suitable sources are available, ambient noise methods are especially useful to simulate a source at each station. Ambient noise surface wave tomography is well established in academic research and has started gaining traction in industry to provide initial coarse resolution images at low cost. There is also great potential in the retrieval of body waves from ambient noise correlations and using these to perform refraction and reflection tomography. Although much more difficult due to the relatively low energy of body waves compared to surface waves (at least on surface sensors), there have been some successful applications. Typically this requires large arrays and long datasets to reveal weak coherencies through stacking waveforms over space and time. Although there remains many challenges, these techniques could revolutionize the seismic exploration industry by reducing the dependence on active sources in mineral and hydrocarbon exploration.

The main weakness of ambient noise processing techniques is the reliance on a diffuse wavefield, which is almost always violated in industrial environments. Since the goal is to extract tiny coherencies through stacking cross-correlation functions over long time periods, any coherent contaminating source will also be amplified. The separation and removal of these coherent sources in real datasets is an especially difficult problem as their number, location and source-time functions can vary. If we wish to successfully apply these techniques in industrial

environments, then this will be an important field of study. This is also relevant to any processing method that involves stacking of waveforms (e.g. beamforming), as seen in Chapter 4.

Another important consideration is the computationally efficient implementation of these methods, especially for real-time monitoring systems. With the majority of mines only equipped with modest processing servers to handle the streaming seismic data, new processing methods will need to prove themselves on this existing hardware to gain any traction.

5.3 Final remarks

Seismology provides many methods for imaging and monitoring the Earth's near surface and while academic research is typically concerned with finding a single best method and then applying it to new datasets, this order is usually reversed in industrial applications. For example, most major mining operations have permanent seismic systems installed that, apart from minor modifications, will remain unchanged over the lifetime of the mine (20+ years). In this case, the properties of the data (e.g quality, array geometry, contaminating sources, etc.) will largely dictate the possible processing techniques (e.g. arrays designed to locate microseismic events using traditional seismic phase-picking methods will not be as well-suited for ambient noise body wave tomography).

Determining the right solution for a given problem depends on achieving a set of goals (e.g. event location, stress monitoring, etc.) given a set of constraints (e.g. environment, budget, time frame etc.). Ideally, the array geometry and data acquisition would then be designed around the chosen processing methods. Even in this case, it is important to evaluate whether the desired processing

methods are still suitable given the acquired data, and be willing to adapt solutions if not.

Effective solutions are pieced together via several building blocks and while it is unlikely to see the exact same solution for two different problems, they commonly share many of the same fundamental building blocks. The goal of this work was to show how the interference (via cross-correlation) and stacking of seismic waveforms can be combined in different ways to create effective solutions for problems faced by today's industries.

Bibliography

[1] N. Myers and J. Kent. “New consumers: the influence of affluence on the environment”. In: *Proceedings of the National Academy of Sciences* 100.8 (2003), pp. 4963–4968.

[2] D. J. Murphy and C. A. Hall. “Energy return on investment, peak oil, and the end of economic growth”. In: *Annals of the New York Academy of Sciences* 1219.1 (2011), pp. 52–72.

[3] S. H. Ali et al. “Mineral supply for sustainable development requires resource governance”. In: *Nature* 543.7645 (2017), p. 367.

[4] T. E. Graedel et al. “On the materials basis of modern society”. In: *Proceedings of the National Academy of Sciences* 112.20 (2015), pp. 6295–6300.

[5] G. Chitombo. “Cave mining: 16 years after Laubscher’s 1994 paper’Cave mining–state of the art’”. In: *Mining Technology* 119.3 (2010), pp. 132–141.

[6] M. J. Sonter. “The technical and economic feasibility of mining the near-earth asteroids”. In: *Acta Astronautica* 41.4-10 (1997), pp. 637–647.

[7] C. Lewicki et al. “Planetary resourcesthe asteroid mining company”. In: *New Space* 1.2 (2013), pp. 105–108.

[8] C. J. Vörösmarty et al. “Global threats to human water security and river biodiversity”. In: *Nature* 467.7315 (2010), p. 555.

[9] M. Jänicke. "Green growth: From a growing eco-industry to economic sustainability". In: *Energy Policy* 48 (2012), pp. 13–21.

[10] S. M. Benson and F. M. Orr. "Carbon dioxide capture and storage". In: *Mrs Bulletin* 33.4 (2008), pp. 303–305.

[11] J. Gibbins and H. Chalmers. "Carbon capture and storage". In: *Energy policy* 36.12 (2008), pp. 4317–4322.

[12] M. Bui et al. "Carbon capture and storage (CCS): the way forward". In: *Energy & Environmental Science* (2018).

[13] R. J. Blakely. *Potential Theory in Gravity and Magnetic Applications*. Cambridge University Press, 1995. DOI: 10.1017/CBO9780511549816.

[14] R. Sheriff and L. Geldart. *Exploration Seismology*. Cambridge University Press, 1995. ISBN: 9781139643115. URL: https://books.google.ca/books?id=wRYgAwAAQBAJ.

[15] M. Salisbury and D. Snyder. "Application of seismic methods to mineral exploration". In: *Mineral Deposits of Canada: A Synthesis of Major Deposit-Types, District Metallogeny, the Evolution of Geological Provinces, and Exploration Methods* 1.5 (2007), pp. 971–982.

[16] A. Malehmir et al. "Seismic methods in mineral exploration and mine planning Introduction". In: *GEOPHYSICS* 77.5 (2012), WC1–WC2. DOI: 10.1190/2012-0724-SPSEIN.1. eprint: https://doi.org/10.1190/2012-0724-SPSEIN.1. URL: https://doi.org/10.1190/2012-0724-SPSEIN.1.

[17] K. M. Keranen et al. "Sharp increase in central Oklahoma seismicity since 2008 induced by massive wastewater injection". In: *Science* 345.6195 (2014), pp. 448–451.

[18] A. J. Mendecki. *Seismic monitoring in mines*. Springer, 1996.

[19] G. Olivier et al. "Investigation of coseismic and postseismic processes using in situ measurements of seismic velocity variations in an underground mine". In: *Geophysical Research Letters* 42.21 (2015), pp. 9261–9269. ISSN: 1944-8007. DOI: 10.1002/2015GL065975.

[20] P. Dales et al. "Interferometric methods for spatio temporal seismic monitoring in underground mines". In: *Geophysical Journal International* 210.2 (2017), p. 731. DOI: 10.1093/gji/ggx189. eprint: /oup/backfile/content_public/journal/gji/210/2/10.1093_gji_ggx189/1/ggx189.pdf. URL: +http://dx.doi.org/10.1093/gji/ggx189.

[21] W. L. Ellsworth. "Injection-induced earthquakes". In: *Science* 341.6142 (2013), p. 1225942.

[22] I. B. Fridleifsson. "Geothermal energy for the benefit of the people". In: *Renewable and sustainable energy reviews* 5.3 (2001), pp. 299–312.

[23] B. Edwards et al. "Seismic monitoring and analysis of deep geothermal projects in St Gallen and Basel, Switzerland". In: *Geophysical Journal International* 201.2 (2015), pp. 1022–1039. DOI: 10.1093/gji/ggv059. eprint: /oup/backfile/content_public/journal/gji/201/2/10.1093/gji/ggv059/2/ggv059.pdf. URL: http://dx.doi.org/10.1093/gji/ggv059.

[24] J. Verdon et al. "Linking microseismic event observations with geomechanical models to minimise the risks of storing CO2 in geological formations". In: *Earth and Planetary Science Letters* 305.1-2 (2011), pp. 143–152.

[25] B. P. Goertz-Allmann et al. “Combining microseismic and geomechanical observations to interpret storage integrity at the In Salah CCS site”. In: *Geophysical Journal International* 198.1 (2014), pp. 447–461.

[26] R. A. Bauer, M. Carney, and R. J. Finley. “Overview of microseismic response to CO 2 injection into the Mt. Simon saline reservoir at the Illinois Basin-Decatur Project”. In: *International Journal of Greenhouse Gas Control* 54 (2016), pp. 378–388.

[27] N. Nakata et al. “Body wave extraction and tomography at Long Beach, California, with ambient-noise interferometry”. In: *Journal of Geophysical Research: Solid Earth* 120.2 (2015), pp. 1159–1173.

[28] F.-C. Lin et al. “High-resolution 3D shallow crustal structure in Long Beach, California: Application of ambient noise tomography on a dense seismic arrayNoise tomography with a dense array”. In: *Geophysics* 78.4 (2013), Q45–Q56.

[29] N. Riahi and P. Gerstoft. “The seismic traffic footprint: Tracking trains, aircraft, and cars seismically”. In: *Geophysical Research Letters* 42.8 (2015), pp. 2674–2681. DOI: 10.1002/2015GL063558. eprint: https://agupubs.onlinelibrary.wiley.com/doi/pdf/10.1002/2015GL063558. URL: https://agupubs.onlinelibrary.wiley.com/doi/abs/10.1002/2015GL063558.

[30] H. Meng and Y. Ben-Zion. “Detection of small earthquakes with dense array data: example from the San Jacinto fault zone, southern California”. In: *Geophysical Journal International* 212.1 (2018), pp. 442–457. DOI: 10.1093/gji/ggx404. eprint: /oup/backfile/content_public/journal/gji/212/

1/10.1093_gji_ggx404/1/ggx404.pdf. URL: http://dx.doi.org/10.1093/gji/ggx404.

[31] S. M. Hansen and B. Schmandt. "Automated detection and location of microseismicity at Mount St. Helens with a Large-N geophone array". In: *Geophysical Research Letters* 42.18 (2015), pp. 7390–7397.

[32] L. Seydoux et al. "Detecting seismic activity with a covariance matrix analysis of data recorded on seismic arrays". In: *Geophysical Journal International* 204.3 (2016), pp. 1430–1442. DOI: 10.1093/gji/ggv531. eprint: /oup/backfile/content_public/journal/gji/204/3/10.1093/gji/ggv531/2/ggv531.pdf. URL: http://dx.doi.org/10.1093/gji/ggv531.

[33] *IRIS Data Distribution Statistics*. URL: http://ds.iris.edu/data/distribution/.

[34] T Utsu. "A statistical study on the occurrence of aftershocks." In: *Geophysical Magazine* 30.4 (1961).

[35] J. F. Claerbout. "Synthesis of a layered medium from its acoustic transmission response". In: *GEOPHYSICS* 33.2 (1968), pp. 264–269. DOI: 10.1190/1.1439927. eprint: http://dx.doi.org/10.1190/1.1439927. URL: http://dx.doi.org/10.1190/1.1439927.

[36] N. M. Shapiro and M. Campillo. "Emergence of broadband Rayleigh waves from correlations of the ambient seismic noise". In: *Geophysical Research Letters* 31.7 (2004). L07614, n/a–n/a. ISSN: 1944-8007. DOI: 10.1029/2004GL019491. URL: http://dx.doi.org/10.1029/2004GL019491.

[37] P. Roux and W. A. Kuperman. "Extracting coherent wave fronts from acoustic ambient noise in the ocean". In: *The Journal of the Acoustical Society of America* 116.4 (2004), pp. 1995–2003. DOI: http://dx.doi.org/10.1121/1.

1797754. URL: http://scitation.aip.org/content/asa/journal/jasa/116/4/10.1121/1.1797754.

[38] K. G. Sabra, P. Roux, and W. A. Kuperman. "Emergence rate of the time-domain Greens function from the ambient noise cross-correlation function". In: *The Journal of the Acoustical Society of America* 118.6 (2005), pp. 3524–3531. DOI: http://dx.doi.org/10.1121/1.2109059.

[39] M. Campillo. "Phase and Correlation in 'Random' Seismic Fields and the Reconstruction of the Green Function". In: *Pure and applied geophysics* 163.2 (2006), pp. 475–502. ISSN: 1420-9136. DOI: 10.1007/s00024-005-0032-8. URL: http://dx.doi.org/10.1007/s00024-005-0032-8.

[40] G. Olivier et al. "Body-wave reconstruction from ambient seismic noise correlations in an underground mine". In: *Geophysics* 80.3 (2015), KS11–KS25. DOI: 10.1190/geo2014-0299.1. eprint: http://dx.doi.org/10.1190/geo2014-0299.1. URL: http://dx.doi.org/10.1190/geo2014-0299.1.

[41] C. Sens-Schonfelder and U. Wegler. "Passive image interferometry and seasonal variations of seismic velocities at Merapi Volcano, Indonesia". In: *Geophysical Research Letters* 33.21 (2006). L21302, n/a–n/a. ISSN: 1944-8007. DOI: 10.1029/2006GL027797. URL: http://dx.doi.org/10.1029/2006GL027797.

[42] F. Brenguier et al. "Towards forecasting volcanic eruptions using seismic noise". In: *Nature Geosci* 1.2 (2008), pp. 126–130. ISSN: 1752-0894. DOI: 10.1038/ngeo104.

[43] O. I. Lobkis and R. L. Weaver. "On the emergence of the Greens function in the correlations of a diffuse field". In: *The Journal of the Acoustical Society of America* 110.6 (2001), pp. 3011–3017. DOI: http://dx.doi.org/10.1121/1.1417528.

[44] R. L. Weaver and O. I. Lobkis. "Diffuse fields in open systems and the emergence of the Greens function (L)". In: *The Journal of the Acoustical Society of America* 116.5 (2004), pp. 2731–2734. DOI: http://dx.doi.org/10.1121/1.1810232. URL: http://scitation.aip.org/content/asa/journal/jasa/116/5/10.1121/1.1810232.

[45] R. Snieder. "Extracting the Green's function from the correlation of coda waves: A derivation based on stationary phase". In: *Phys. Rev. E* 69 (4 2004), p. 046610. DOI: 10.1103/PhysRevE.69.046610.

[46] P. Dales, P. Audet, and G. Olivier. "Seismic Interferometry Using Persistent Noise Sources for Temporal Subsurface Monitoring". In: *Geophysical Research Letters* 44.21 (2017).

[47] R. M. Allen and H. Kanamori. "The Potential for Earthquake Early Warning in Southern California". In: *Science* 300.5620 (2003), pp. 786–789. ISSN: 0036-8075. DOI: 10.1126/science.1080912.

[48] R. V. Allen. "Automatic earthquake recognition and timing from single traces". In: *Bulletin of the Seismological Society of America* 68.5 (1978), pp. 1521–1532. eprint: http://www.bssaonline.org/content/68/5/1521.full.pdf+html.

[49] L Geiger. "Probability method for the determination of earthquake epicenters from the arrival time only". In: *Bulletin of St. Louis University* 8 (1912),

pp. 60–71. eprint: http://www.bssaonline.org/content/68/5/1521.full.pdf+html.

[50] C. Knapp and G. Carter. "The generalized correlation method for estimation of time delay". In: *IEEE Transactions on Acoustics, Speech, and Signal Processing* 24.4 (1976), pp. 320–327. ISSN: 0096-3518. DOI: 10.1109/TASSP.1976.1162830.

[51] N. Marchand. "Error Distributions of Best Estimate of Position from Multiple Time Difference Hyperbolic Networks". In: *IEEE Transactions on Aerospace and Navigational Electronics* ANE-11.2 (1964), pp. 96–100. ISSN: 0096-1957. DOI: 10.1109/TANE.1964.4502170.

[52] K. Obara. "Nonvolcanic Deep Tremor Associated with Subduction in Southwest Japan". In: *Science* 296.5573 (2002), pp. 1679–1681. ISSN: 0036-8075. DOI: 10.1126/science.1070378.

[53] N. M. Shapiro, M. H. Ritzwoller, and G. D. Bensen. "Source location of the 26 sec microseism from cross-correlations of ambient seismic noise". In: *Geophysical Research Letters* 33.18 (2006). L18310, n/a–n/a. ISSN: 1944-8007. DOI: 10.1029/2006GL027010.

[54] W. Hahn and S. Tretter. "Optimum processing for delay-vector estimation in passive signal arrays". In: *IEEE Transactions on Information Theory* 19.5 (1973), pp. 608–614. ISSN: 0018-9448. DOI: 10.1109/TIT.1973.1055077.

[55] M. Wax and T. Kailath. "Optimum localization of multiple sources by passive arrays". In: *IEEE Transactions on Acoustics, Speech, and Signal Processing* 31.5 (1983), pp. 1210–1217. ISSN: 0096-3518. DOI: 10.1109/TASSP.1983.1164183.

[56] H. P. Bucker. "Use of calculated sound fields and matchedfield detection to locate sound sources in shallow water". In: *The Journal of the Acoustical Society of America* 59.2 (1976), pp. 368–373. DOI: 10.1121/1.380872. eprint: http://dx.doi.org/10.1121/1.380872. URL: http://dx.doi.org/10.1121/1.380872.

[57] W. Kuperman and G. Turek. "Matched Field Acoustics". In: *Mechanical Systems and Signal Processing* 11.1 (1997), pp. 141 –148. ISSN: 0888-3270. DOI: http://dx.doi.org/10.1006/mssp.1996.0066. URL: http://www.sciencedirect.com/science/article/pii/S0888327096900667.

[58] E. Cros et al. "Locating hydrothermal acoustic sources at Old Faithful Geyser using Matched Field Processing". In: *Geophysical Journal International* 187.1 (2011), p. 385. DOI: 10.1111/j.1365-246X.2011.05147.x. eprint: /oup/backfile/Content_public/Journal/gji/187/1/10.1111/j.1365-246X.2011.05147.x/3/187-1-385.pdf. URL: +http://dx.doi.org/10.1111/j.1365-246X.2011.05147.x.

[59] M. Corciulo et al. "Multiscale matched-field processing for noise-source localization in exploration geophysics". In: *GEOPHYSICS* 77.5 (2012), KS33–KS41. DOI: 10.1190/geo2011-0438.1. eprint: http://dx.doi.org/10.1190/geo2011-0438.1. URL: http://dx.doi.org/10.1190/geo2011-0438.1.

[60] H. Kao and S.-J. Shan. "The Source-Scanning Algorithm: mapping the distribution of seismic sources in time and space". In: *Geophysical Journal International* 157.2 (2004), pp. 589–594. DOI: 10.1111/j.1365-246X.2004.02276.x. eprint: http://gji.oxfordjournals.org/content/157/2/589.

full.pdf+html. URL: http://gji.oxfordjournals.org/content/157/2/589.abstract.

[61] J. Wassermann. "Locating the sources of volcanic explosions and volcanic tremor at Stromboli volcano (Italy) using beam-forming on diffraction hyperboloids". In: *Physics of the Earth and Planetary Interiors* 104.1 (1997), pp. 271 –281. ISSN: 0031-9201. DOI: http://dx.doi.org/10.1016/S0031-9201(97)00041-1. URL: http://www.sciencedirect.com/science/article/pii/S0031920197000411.

[62] J. DiBiase. "A High-Accuracy, Low-Latency Technique for Talker Localization in Reverberant Environments Using Microphone Arrays". PhD thesis. The address of the publisher: Brown University, May 2000.

[63] J. H. DiBiase, H. F. Silverman, and M. S. Brandstein. "Robust Localization in Reverberant Rooms". In: *Microphone Arrays: Signal Processing Techniques and Applications*. Ed. by M. Brandstein and D. Ward. Berlin, Heidelberg: Springer Berlin Heidelberg, 2001, pp. 157–180. ISBN: 978-3-662-04619-7. DOI: 10.1007/978-3-662-04619-7_8.

[64] S. Ballmer et al. "Ambient seismic noise interferometry in Hawai'i reveals long-range observability of volcanic tremor". In: *Geophysical Journal International* 194.1 (2013), pp. 512–523. DOI: 10.1093/gji/ggt112. eprint: http://gji.oxfordjournals.org/content/194/1/512.full.pdf+html. URL: http://gji.oxfordjournals.org/content/194/1/512.abstract.

[65] D. Droznin et al. "Detecting and locating volcanic tremors on the Klyuchevskoy group of volcanoes (Kamchatka) based on correlations of continuous seismic records". In: *Geophysical Journal International* 203.2 (2015), pp. 1001–1010. DOI: 10.1093/gji/ggv342. eprint: http://gji.oxfordjournals.

org/content/203/2/1001.full.pdf+html. URL: http://gji.oxfordjournals.org/content/203/2/1001.abstract.

[66] E. Ruigrok, S. Gibbons, and K. Wapenaar. "Cross-correlation beamforming". In: *Journal of Seismology* (2016), pp. 1–14. ISSN: 1573-157X. DOI: 10.1007/s10950-016-9612-6. URL: http://dx.doi.org/10.1007/s10950-016-9612-6.

[67] M. Afanasiev et al. *Salvus: A high-performance package for full waveform modelling and inversion from laboratory to global scales*. 0.0.1-475-gc87fc6d1. Mar. 2017. DOI: 10.5905/ethz-1007-88. URL: https://doi.org/10.5905/ethz-1007-88.

[68] G. D. Bensen et al. "Processing seismic ambient noise data to obtain reliable broad-band surface wave dispersion measurements". In: *Geophysical Journal International* 169.3 (2007), pp. 1239–1260. ISSN: 1365-246X. DOI: 10.1111/j.1365-246X.2007.03374.x. URL: http://dx.doi.org/10.1111/j.1365-246X.2007.03374.x.

[69] Z. Chen, P. Gerstoft, and P. D. Bromirski. "Microseism source direction from noise cross-correlation". In: *Geophysical Journal International* 205.2 (2016), p. 810. DOI: 10.1093/gji/ggw055. eprint: /oup/backfile/Content_public/Journal/gji/205/2/10.1093/gji/ggw055/2/ggw055.pdf. URL: +http://dx.doi.org/10.1093/gji/ggw055.

[70] J. Groos, S. Bussat, and J. Ritter. "Performance of different processing schemes in seismic noise cross-correlations". In: *Geophysical Journal International* 188.2 (2012), pp. 498–512. ISSN: 1365-246X. DOI: 10.1111/j.1365-246X.2011.05288.x. URL: http://dx.doi.org/10.1111/j.1365-246X.2011.05288.x.

[71] M. Wathelet et al. "Array performances for ambient vibrations on a shallow structure and consequences over Vs inversion". In: *Journal of Seismology* 12.1 (2008), pp. 1–19. ISSN: 1573-157X. DOI: 10.1007/s10950-007-9067-x. URL: http://dx.doi.org/10.1007/s10950-007-9067-x.

[72] H. Do, H. F. Silverman, and Y. Yu. "A Real-Time SRP-PHAT Source Location Implementation using Stochastic Region Contraction(SRC) on a Large-Aperture Microphone Array". In: *2007 IEEE International Conference on Acoustics, Speech and Signal Processing - ICASSP '07*. Vol. 1. 2007, pp. I–121–I–124. DOI: 10.1109/ICASSP.2007.366631.

[73] M. F. Berger and H. F. Silverman. "Microphone array optimization by stochastic region contraction". In: *IEEE Transactions on Signal Processing* 39.11 (1991), pp. 2377–2386. ISSN: 1053-587X. DOI: 10.1109/78.97993.

[74] H. Do and H. F. Silverman. "SRP-PHAT methods of locating simultaneous multiple talkers using a frame of microphone array data". In: *2010 IEEE International Conference on Acoustics, Speech and Signal Processing*. 2010, pp. 125–128. DOI: 10.1109/ICASSP.2010.5496133.

[75] J.-P. Mercier et al. "Evolution of a block cave from time-lapse passive source body-wave traveltime tomography". In: *Geophysics* 80.2 (2015), WA85–WA97. ISSN: 0016-8033. DOI: 10.1190/geo2014-0155.1. eprint: http://geophysics.geoscienceworld.org/content/80/2/WA85.full.pdf. URL: http://geophysics.geoscienceworld.org/content/80/2/WA85.

[76] C. Hadziioannou et al. "Stability of monitoring weak changes in multiply scattering media with ambient noise correlation: Laboratory experiments". In: *The Journal of the Acoustical Society of America* 125.6 (2009),

pp. 3688–3695. DOI: 10.1121/1.3125345. eprint: http://dx.doi.org/10.1121/1.3125345. URL: http://dx.doi.org/10.1121/1.3125345.

[77] B. Froment et al. "Estimation of the effect of nonisotropically distributed energy on the apparent arrival time in correlations". In: *GEOPHYSICS* 75.5 (2010), SA85–SA93. DOI: 10.1190/1.3483102. eprint: https://doi.org/10.1190/1.3483102. URL: https://doi.org/10.1190/1.3483102.

[78] F Brenguier et al. "Mapping pressurized volcanic fluids from induced crustal seismic velocity drops". In: *Science* 345.6192 (2014), pp. 80–82.

[79] G. Olivier et al. "Monitoring the stability of tailings dam walls with ambient seismic noise". In: *The Leading Edge* (2017).

[80] C. Donaldson et al. "Relative seismic velocity variations correlate with deformation at Kīlauea volcano". In: *Science advances* 3.6 (2017), e1700219.

[81] A. Grêt, R. Snieder, and U. Özbay. "Monitoring in situ stress changes in a mining environment with coda wave interferometry". In: *Geophysical Journal International* 167.2 (2006), pp. 504–508. ISSN: 1365-246X. DOI: 10.1111/j.1365-246X.2006.03097.x. URL: http://dx.doi.org/10.1111/j.1365-246X.2006.03097.x.

[82] A. E. Rogers et al. "Very-long-baseline radio interferometry: The Mark III system for geodesy, astrometry, and aperture synthesis". In: *Science* 219.4580 (1983), pp. 51–54.

[83] E. T. Brown. *Block caving geomechanics*. Julius Kruttschnitt Mineral Research Center, JKMRC Monograph Series in Mining and Mineral Processing., 2007.

[84] G. Poupinet, W. L. Ellsworth, and J. Frechet. "Monitoring velocity variations in the crust using earthquake doublets: An application to the Calaveras Fault, California". In: *Journal of Geophysical Research: Solid Earth* 89.B7 (1984), pp. 5719–5731. ISSN: 2156-2202. DOI: 10.1029/JB089iB07p05719. URL: http://dx.doi.org/10.1029/JB089iB07p05719.

[85] E. Larose et al. "Locating and characterizing a crack in concrete with diffuse ultrasound: A four-point bending test". In: *The Journal of the Acoustical Society of America* 138.1 (2015), pp. 232–241. DOI: 10.1121/1.4922330. eprint: http://dx.doi.org/10.1121/1.4922330. URL: http://dx.doi.org/10.1121/1.4922330.

[86] G. Olivier and F. Brenguier. "Interpreting seismic velocity changes observed with ambient seismic noise correlations". In: *Interpretation* 4.3 (2016), SJ77–SJ85.

[87] J. Vandemeulebrouck, P. Roux, and E. Cros. "The plumbing of Old Faithful Geyser revealed by hydrothermal tremor". In: *Geophysical Research Letters* 40.10 (2013), pp. 1989–1993. ISSN: 1944-8007. DOI: 10.1002/grl.50422. URL: http://dx.doi.org/10.1002/grl.50422.

[88] P. Gerstoft et al. "Global P, PP, and PKP wave microseisms observed from distant storms". In: *Geophysical Research Letters* 35.23 (2008). L23306, n/a–n/a. ISSN: 1944-8007. DOI: 10.1029/2008GL036111. URL: http://dx.doi.org/10.1029/2008GL036111.

[89] J. Zhang, P. Gerstoft, and P. D. Bromirski. "Pelagic and coastal sources of P-wave microseisms: Generation under tropical cyclones". In: *Geophysical Research Letters* 37.15 (2010). L15301, n/a–n/a. ISSN: 1944-8007. DOI: 10.1029/2010GL044288. URL: http://dx.doi.org/10.1029/2010GL044288.

[90] Z. Li et al. "High-resolution seismic event detection using local similarity for Large-N arrays". In: *Scientific reports* 8.1 (2018), p. 1646.

[91] A. Inbal, R. W. Clayton, and J.-P. Ampuero. "Imaging widespread seismicity at midlower crustal depths beneath Long Beach, CA, with a dense seismic array: Evidence for a depth-dependent earthquake size distribution". In: *Geophysical Research Letters* 42.15 (2015), pp. 6314–6323.

[92] J. T. Rutledge and W. S. Phillips. "Hydraulic stimulation of natural fractures as revealed by induced microearthquakes, Carthage Cotton Valley gas field, east Texas Hydraulic Stimulation of Natural Fractures". In: *Geophysics* 68.2 (2003), pp. 441–452.

[93] L. Eisner et al. "Beyond the dots in the box: Microseismicity-constrained fracture models for reservoir simulation". In: *The Leading Edge* 29.3 (2010), pp. 326–333.

[94] G. Beskardes et al. "A comparison of earthquake backprojection imaging methods for dense local arrays". In: *Geophysical Journal International* 212.3 (2017), pp. 1986–2002.

[95] A. Aubry and A. Derode. "Random matrix theory applied to acoustic backscattering and imaging in complex media". In: *Physical review letters* 102.8 (2009), p. 084301.

[96] L. Eisner et al. "The peak frequency of direct waves for microseismic events". In: *Geophysics* 78.6 (2013), A45–A49.

[97] J. P. Verdon et al. "Comparison of geomechanical deformation induced by megatonne-scale CO2 storage at Sleipner, Weyburn, and In Salah". In: *Proceedings of the National Academy of Sciences* 110.30 (2013), E2762–E2771.

[98] A. L. Stork et al. "Assessing the potential to use repeated ambient noise seismic tomography to detect CO 2 leaks: Application to the Aquistore storage site". In: *International Journal of Greenhouse Gas Control* 71 (2018), pp. 20–35.